

## Simple model for bifurcations ranging up to chaos in thermal lens oscillations and associated phenomena

G. Gouesbet

*Laboratoire d'Energétique des Systèmes et Procédés,  
Institut National des Sciences Appliquées de Rouen, Boîte Postale 08,  
76131 Mont-Saint-Aignan CEDEX, France*

(Received 15 February 1990; revised manuscript received 2 July 1990)

A very simple model is designed to understand dynamical states and bifurcations ranging up to chaos in thermal lens oscillations and associated hot-wire experiments. The present system is governed by partial-derivative equations in the case of bulk liquid and also at a free surface which is a boundary of the liquid. It is reduced to a set of three nonlinear ordinary differential equations with two control parameters to be studied within the framework of the theory of nonlinear dynamical systems. The model may evolve to chaos in three domains of the parameter plane. Metric and dynamical properties (generalized dimensions and entropies, and associated singularity spectra) of a (presumably) strange chaotic attractor produced by the model are determined. The overall good and sometimes striking agreement between the model and previously reported experimental results shows that we have reached a fair understanding of the experimental phenomena, much better than what has been hitherto possible.

### I. INTRODUCTION

The study of nonlinear dissipative dynamical systems exhibiting a rich variety of behaviors, from equilibria and limit cycles, to chaos and turbulence, has been a subject of increasing interest. A rather comprehensive background may be acquired from textbooks such as those by Guckenheimer and Holmes,<sup>1</sup> Thompson and Stewart,<sup>2</sup> Devaney,<sup>3</sup> Bergé, Pomeau, and Vidal,<sup>4</sup> and from an increasingly prolific literature.

Among hydrodynamic instabilities pertaining to the above framework such as Rayleigh-Bénard and Bénard-Marangoni effects,<sup>5</sup> this paper is devoted to a new phenomenon, namely, thermal lens oscillations (which we also call optical heartbeats, or "*coeur d'anneaux*" in French), observed for the first time by Jakeman, Pike, and Vaughan<sup>6</sup> to our knowledge, rediscovered independently within our group,<sup>7</sup> and systematically investigated since then.

Optical heartbeats can be produced when a laser beam propagates horizontally below a free surface, or vertically upwards.<sup>8,9</sup> In associated hot-wire experiments, heating is carried out with a hot wire instead of a laser.<sup>10,11</sup> Complex behavior may be observed, including steady states (equilibrium), limit cycles, quasiperiodicity with mode lockings, Feigenbaum cascades, hysteresis associated with the coexistence of multiple attractors, and chaos.

Rigorous equations of the system are coupled partial-derivative equations (PDE's) governing the liquid bulk and the free surface, supplemented by boundary conditions at rigid walls. PDE's at the free surface play a two-fold role: they have to be solved as a part of the problem but they simultaneously introduce boundary conditions for the bulk. The resulting problem is of tremendous difficulty increased by a lack of symmetry.

The orbit of the system evolves in an infinite-

dimensional phase space associated with PDE's. However, due to dissipation, the long-term recurrent motions settle down on finite-dimensional objects embedded in finite-dimensional phase spaces. Then, we may in principle replace PDE's by a finite set of coupled first-order ordinary differential equations (ODE's), i.e., by a dynamical system of the form  $\dot{X} = F(X)$ , in which  $X$  is a vector evolving in an  $n$ -dimensional phase space, the flow being generated by vector field  $F$ .

In this paper we design a simple model of thermal lens oscillations [heartbeat experiments (HBE's)] and associated hot-wire experiments (HWE's) by reducing the problem defined by PDE's to an ODE's dynamical system. Nevertheless, the implementation of a systematic reduction procedure (Galerkin method, reduction to normal forms<sup>12,13</sup>) is in practice forbidden or at least excessively difficult due to the lack of symmetry we mentioned above. We shall rather rely on another approach by using several ingredients including a qualitative understanding of phenomena, dimensional analysis, and simple concepts from dynamical systems theory. The final outcome is a two-parameter three-dimensional vector field representing a nonlinear coupling between a mechanical oscillator associated with a free surface and a thermal "oscillator" associated with a heat source. Comparisons between the model and experimental results will lead us to the conclusion that we attained a precise understanding of HBE's and HWE's, at least much better than hitherto possible.

The paper is organized as follows. Section II is devoted to a brief review of our present knowledge concerning HBE's and HWE's. Section III establishes the model in two main steps, leading first to a one-parameter two-dimensional dynamical system to understand a supercritical Hopf bifurcation observed in both HBE's and HWE's, then to a two-parameter three-dimensional dynamical

system to understand secondary instabilities in HBE's. Model numerical results and comparisons with experimental data are provided in Sec. IV. Finally, for the purpose of later comparisons with experiments, Sec. V is devoted to the metric and dynamical characterization (generalized dimensions and entropies, and associated singularity spectra) of a (presumably) strange chaotic attractor generated by the model.

## II. HBE'S AND HWE'S: EXPERIMENTAL SECTION

This section is a brief summary of a recent review paper concerning HBE's and HWE's.<sup>14</sup> Thermal lenses may be produced when a laser beam propagates in an absorbing liquid contained in a cell. They provoke a divergence of the beam and the creation of a ring pattern resulting from optical aberrations of a thermal lens. When a laser beam of power  $P$  propagates horizontally at a distance  $d$  below the free surface, the outgoing beam may exhibit various oscillatory behaviors in a domain of the control parameter plane  $(P, d)$ . These luminous phenomena are called optical heartbeats and result from oscillatory convection in the cell (thermal lens oscillations) associated with propagating waves at the free surface. Optical heartbeats may also be produced with the laser beam propagating vertically upwards, but this case has not been extensively investigated because it exhibits only one bifurcation from steady to oscillatory states.<sup>7,8</sup> Typical laser powers for quantitative experiments are between 100 and 500 mW in Refs. 9 and 15 but thermal lens oscillations may already be obtained at small laser powers of  $\approx 5$  mW.<sup>11,16</sup>

References 9 and 15 extensively report on quantitative

HBE's in the case of an argon-ion laser propagating horizontally below a free surface in a cell filled with a Rhodorsil silicon oil colored with a dye. A photodiode tracks the variations of the luminous intensity of the outgoing beam. The signal is observed in the time domain or in the frequency domain by using a fast-Fourier-transform (FFT) spectrum analyzer. The state diagram obtained in the control parameter plane  $(P, d)$  is shown in Fig. 1.

Outside curve BL1 (bifurcation line number one), the system is steady (zone S). It is unsteady inside (zone US). This bifurcation line indicates the onset of oscillatory behavior through a supercritical Hopf bifurcation (although a small amount of subcriticality revealed by hysteresis phenomena might exist, mainly for a large value of  $d$ , according to more recent unconfirmed experiments in HWE's). In the unsteady zone (US), several kinds of behavior are observed: periodic with one fundamental frequency (zone P), periodic with subharmonics corresponding to Feigenbaum cascades in zone PD (period doubling), and quasiperiodic with two fundamental frequencies in zones QP1 and QP2 which are probably connected together (measurements have not been performed for  $P$  between about 200 and 300 mW). Frequency lockings are also observed when the two fundamental frequencies of the quasiperiodic signals become commensurable. In the hysteresis zone (H), the system may be attracted either to a periodic or to a quasiperiodic state, depending on whether we proceed by decreasing or increasing  $d$  for a given  $P$ . Chaos may be observed although it does not appear in Fig. 1 (Ref. 8, and unpublished observations).

In HWE's laser heating is replaced by hot-wire heating.<sup>17,10,11</sup> Most of the experiments have been carried out by using a temperature-controlled hot wire.<sup>10,11</sup> Driving measured thermal force is then  $\Delta T$ , the temperature difference between hot-wire temperature and ambient

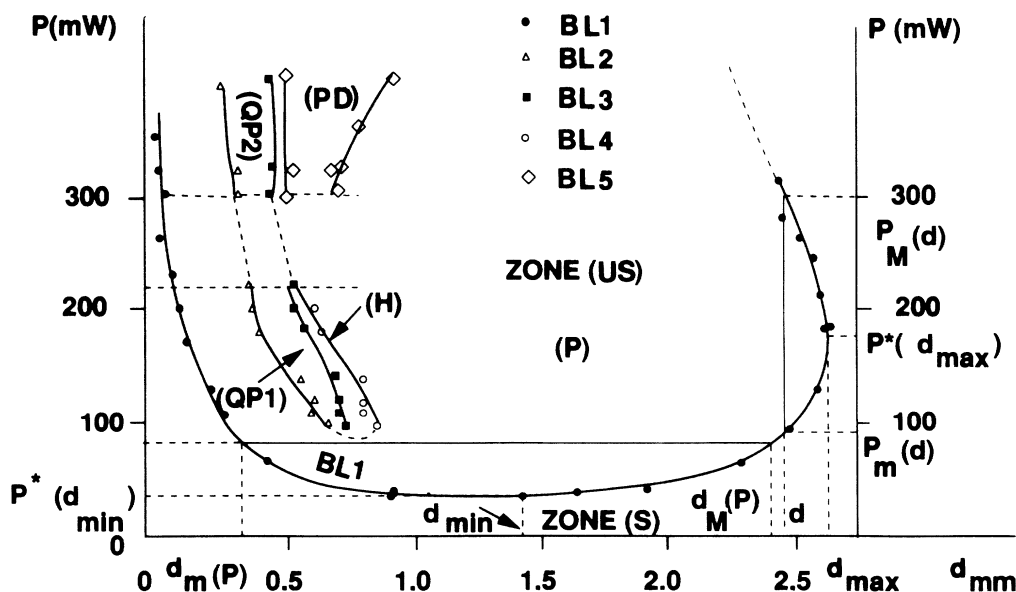


FIG. 1. HBE's state diagram in control parameter plane  $(P, d)$ .  $P$  is laser power,  $d$  is a distance between laser beam and free surface.

temperature. When  $\Delta T$  is increased from 0, we observe a steady convection and a steady deformation of free surface up to a critical value  $\Delta T_*$  for the onset of oscillatory behavior. Measurements of critical quantities (critical  $\Delta T_*$ 's and associated critical frequencies  $f_*$ 's) have been carried out for four silicon oils. Critical quantities versus  $d$  depend on the oil but, when appropriately presented in terms of dimensionless values, the different profiles collapse reasonably well to single "universal" curves.<sup>18</sup> There also exists a quantitative similarity between HWE's and HBE's for the first bifurcation from steady to periodic.<sup>9</sup>

Exemplifying results are displayed in Fig. 2 showing critical frequencies  $f_*$  versus critical temperature differences  $\Delta T_*$ . These values are obtained by varying  $d$ . There exists a  $d = d_{\min}$  at which  $\Delta T_*$  has a minimum  $\Delta T_*(d_{\min})$ . In each curve of Fig. 2, the values  $\Delta T_*(d_{\min})$  correspond to a sharp separation between a nearly horizontal branch and a rather vertical branch. This fact strongly suggests that two different mechanisms may be at work, depending on whether  $d$  is smaller or larger than  $d_{\min}$ , and will be used in designing the model. It is also confirmed by the observation that, prior to the onset of oscillations, the free surface is depressed for  $d < d_{\min}$  (typical of the Marangoni effect) while it is elevated for  $d > d_{\min}$  (typical of buoyancy-driven convection).<sup>19</sup>

The qualitative analogy between HBE's and HWE's is obvious. In each case, oscillatory instabilities are triggered by heating below the free surface. As mentioned before, there is also a quantitative similarity for the onset of oscillatory behavior concerning both  $\phi_*(d)$  and  $f_*(d)$ , in which  $\phi$  stands for either  $P$  (HBE's) or  $\Delta T$  (HWE's).<sup>9</sup> However, no secondary instabilities after the Hopf bifurcation are observed in HWE's. The reason for this difference of behavior between HBE's and HWE's will be discussed later when the model is developed (Sec. III I).

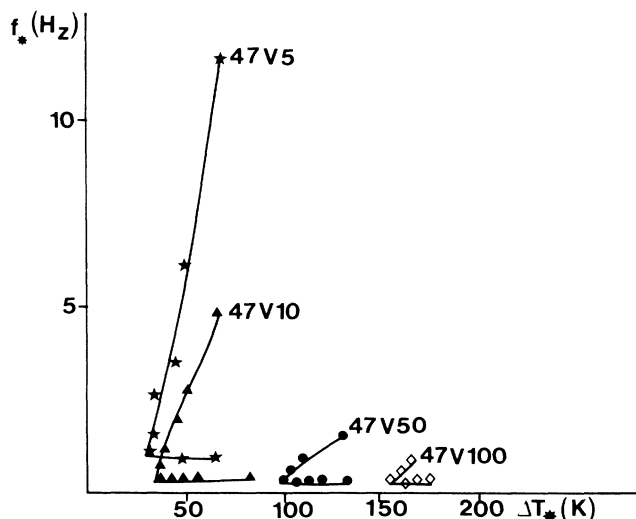


FIG. 2. HWE's. Critical frequencies  $f_*$  vs critical temperature differences  $\Delta T_*$  for four silicon oils. 47Vi are oil labels.

### III. MODEL

#### A. Generalities

A rigorous solution of the problem can only be gained from numerical simulation. This task has been undertaken for HWE's (Ref. 20) but is not completed. In a second approach, we examined a possible analogy between (a) HBE's and HWE's and (b) the case when a horizontal liquid layer loses its stability, evolving from a motionless liquid layer to an oscillatory convective one, under simultaneous surface tension and coupled buoyancy effects.<sup>21-23</sup> The simultaneous effect of shear has been included in the analysis later on.<sup>24</sup> Although this approach provided significant results for the case of the horizontal liquid layer in its own right, it has been found disappointing in understanding HBE's and HWE's. Furthermore, in any case, the aforementioned approaches heavily rely on lengthy algebra and intense computer programming, hiding the essence of the physics. Now, we instead develop a simple illuminating model reducing the original PDE's to a nonlinear dynamical system in  $\mathbb{R}^3$ . In doing so, we shall be inevitably forced to progressively introduce some arbitrariness. Therefore we shall sometimes have to be content with a resemblance between the model and the experimental results. This notion of resemblance may be given a precise formulation by invoking the concepts of structural stability and topological equivalence of attracting sets in phase space (see Ref. 1, Sec. 5-4, and Ref. 2, Sec. IV-7).

#### B. Marginal condition for the onset of oscillatory behavior

We set that heat is transported from the heat source to the free surface with a characteristic time  $t_1$ . When a hot blob reaches the surface, it is disrupted by the Marangoni effect<sup>5</sup> with a characteristic time  $t_2$ . The condition  $t_1 \gg t_2$  is sufficient for the process to take a cyclical character, with upward heat transport followed by heat disruption at the surface and convective cooling below. Marangoni disruption results in waves which propagate on the surface in the direction parallel to the wire. Conversely, if  $t_1 \ll t_2$ , heat is rapidly supplied to the surface and gently removed. We may then expect the appearance of a steady balance.

We therefore introduce the ratio of characteristic times:

$$R = t_1/t_2 \quad (1)$$

and set that the marginal condition for the onset of oscillatory behavior is given by a critical value of this ratio:

$$R_* = \chi, \quad (2)$$

in which the precise value of  $\chi$  is unknown.

#### C. Characteristic times

Evaluation of characteristic times is different whether  $d$  is small or large (remember the comments of Fig. 2).

(a) For  $d$  small (free surface depressed), we assume that

$t_1$  is a conduction time:

$$t_1 = k_1 d^2 / K_T, \quad (3)$$

in which  $K_T$  is the liquid thermal diffusivity and  $k_1$  an unknown dimensionless constant.

For the Marangoni disruption time we have

$$t_2 = k_2 d / V_M, \quad (4)$$

where  $k_2$  is another unknown dimensionless constant and  $V_M$  is a Marangoni velocity:

$$V_M = \frac{|\Gamma| \Delta T}{\mu}. \quad (5)$$

Here,  $\Gamma$  is the derivative of surface tension with respect to temperature  $T$ ,  $\mu$  the liquid dynamic viscosity, and  $\Delta T$  is the temperature difference between heat source temperature and ambient temperature above the free surface. Hence

$$t_2 = k_2 \mu d / (|\Gamma| \Delta T). \quad (6)$$

(b) When  $d$  is large (free surface elevated), we assume that heat transport is essentially convective. Then  $t_1$  is  $d/U$  in which  $U$  is a velocity convection. Both in HBE's and HWE's, heating sources produce hot blobs going upward due to buoyancy. We consider that these blobs are physical entities on which a downward drag force is exerted by the surrounding fluid and assume that this drag may be approximately evaluated by using Stokes's law. Velocity convection  $U$  is then evaluated as the result of a balance between upward buoyancy lift and downward Stokes drag. Detailed discussion is, however, a bit longer than for  $d$  small. We obtain<sup>25,26</sup>

$$t_1 = K_1 \left[ \frac{\mu}{\alpha_T \rho_0 g} \right]^{1/3} \frac{d}{K_T^{2/3} \Delta T^{1/3}} \exp(-\mathcal{N}_{Ra}), \quad (7)$$

in which  $\alpha_T$  is thermal expansivity,  $\rho_0$  is density at reference temperature  $T_0$ ,  $g$  is gravity modulus,  $K_1$  a new unknown dimensionless constant, and  $\mathcal{N}_{Ra}$  is the Rayleigh number defined by

$$\mathcal{N}_{Ra} = \frac{g \alpha_T d^3 \rho_0 \Delta T}{\mu K_T}. \quad (8)$$

$t_2$  is still a Marangoni time which is, however, now given by<sup>25</sup>

$$t_2 = K_2 \left[ \frac{\alpha_T \rho_0 g \mu^2}{K_T \Delta T^2} \right]^{1/3} \frac{d^2}{|\Gamma|}, \quad (9)$$

in which we introduced a last unknown dimensionless constant  $K_2$ .

Introducing the Marangoni number

$$\mathcal{N}_{Ma} = \frac{|\Gamma| \Delta T d}{\mu K_T}, \quad (10)$$

we then readily find that the ratio  $R$  of characteristic times is given by

$$R = \frac{k_1}{k_2} \frac{|\Gamma| \Delta T d}{\mu K_T} = \frac{k_1}{k_2} \mathcal{N}_{Ma} = \frac{k_1}{k_2} V_M^+, \quad \text{small } d \quad (11)$$

$$R = \frac{K_1}{K_2} \frac{|\Gamma|}{d} \left[ \frac{\Delta T}{\mu \alpha_T^2 \rho_0^2 g^2 K_T} \right]^{1/3} \exp \left[ - \frac{g \alpha_T d^3 \rho_0 \Delta T}{\mu K_T} \right] \\ = \frac{K_1}{K_2} \frac{\mathcal{N}_{Ma}}{\mathcal{N}_{Ra}^{2/3}} \exp(-\mathcal{N}_{Ra}), \quad \text{large } d \quad (12)$$

in which  $V_M^+ = V_M t_1 / d$  is Marangoni velocity  $V_M$  made dimensionless by using  $d$  as a unit of length and  $t_1$  as a unit of time. Consequently,  $R$  may be expressed in terms of thermophysical properties or, alternatively, in terms of the two dimensionless groups ( $\mathcal{N}_{Ma}, \mathcal{N}_{Ra}$ ) relevant to the problem.

#### D. Another dimensionless formulation

Although the formulation above is dimensionless, it is not appropriate to a later comparison with experiments because it contains four unknown elements in evaluating characteristic times and a fifth one which is the critical value of ratio  $R$ . We therefore need another dimensionless formulation. For the propose, we introduce

$$A = \frac{\mu K_T (\alpha_T \rho_0 g)^2}{|\Gamma|^3}, \quad (13)$$

$$B = \frac{\alpha_T \rho_0 g}{\mu K_T}, \quad (14)$$

leading to

$$\mathcal{N}_{Ma} = \frac{B^{2/3}}{A^{1/3}} \Delta T d, \quad (15)$$

$$\mathcal{N}_{Ra} = B \Delta T d^3. \quad (16)$$

Equations (15) and (16) express the two main dimensionless groups ( $\mathcal{N}_{Ma}, \mathcal{N}_{Ra}$ ) in terms of  $A$  and  $B$  (depending on thermophysical properties) and of the two control parameters  $\Delta T$  and  $d$  driving the instabilities.

The condition for marginal stability may then be rewritten for large  $d$  as

$$\gamma \Delta T_*^{1/3} \exp(-B d^3 \Delta T_*) = A^{1/3} d, \quad (17)$$

in which the critical  $R_* = \chi$  has been absorbed in  $\gamma$  according to

$$\gamma = \frac{K_1}{K_2 \chi}. \quad (18)$$

Equation (17) has no solution for  $d > d_{\max}$ , where  $d_{\max}$  is given below. For  $d < d_{\max}$ , there are two critical values  $\Delta T_*^1$  and  $\Delta T_*^2$  limiting a  $\Delta T$  domain in which oscillatory behavior will occur, in agreement with experiments (see Fig. 1 in which  $\Delta T$  is actually linked to  $P$ ). When  $d$  increases, the difference  $|\Delta T_*^1 - \Delta T_*^2|$  decreases down to 0 at  $d = d_{\max}$ . For  $d$  larger than  $d_{\max}$ , the steady state is always stable. We readily find that  $d_{\max}$  and  $\Delta T_*(d_{\max})$  are given by

$$d_{\max} = \frac{\sqrt{\gamma}}{(3eAB)^{1/6}}, \quad (19)$$

$$\Delta T_*(d_{\max}) = \frac{1}{\gamma^{3/2}} \left[ \frac{eA}{3B} \right]^{1/2}. \quad (20)$$

Equations (19) and (20) provide us with two well-defined scales to make  $d$  and  $\Delta T$  dimensionless. In HBE's,  $\Delta T, \Delta T_*$  are replaced by laser powers  $P, P_*$  which is justified by the quantitative analogy between HBE's and WHE's.<sup>9</sup> We consequently introduce

$$x = d/d_{\max}, \quad (21)$$

$$y = \Delta T/\Delta T_*(d_{\max}) = P/P_*(d_{\max}). \quad (22)$$

### E. Critical $y_*$ 's and matching

Expressed in terms of the dimensionless  $x$  and  $y$ , the marginal stability condition is

$$y_* = \delta \left[ \frac{9}{e} \right]^{1/3} / x, \quad \text{small } d \quad (23)$$

$$\frac{(ey_*)^{1/3}}{x} \exp(-\frac{1}{3}y_*x^3) = 1, \quad \text{large } d \quad (24)$$

in which we have

$$\delta = \frac{k_1}{k_2} \gamma \chi = \frac{k_1 K_1}{k_2 K_2}. \quad (25)$$

We observe that (23) and (24) do not contain the unknown  $\chi$  any more and that the other four unknown elements are now incorporated in a single unknown element  $\delta$ . Also, thermophysical properties have been eliminated in the process. Hence our model leads to a universal profile for the onset of oscillatory behavior, in agreement with the experiments carried out so far.<sup>9,18</sup> We notice that (24) is implicit and must be solved numerically, leading to two critical values  $y_*^1$  and  $y_*^2$  ( $y_*^1 < y_*^2$ ) for a given  $x$ , up to  $x=1$  ( $d=d_{\max}$ ) where  $y_*^1 = y_*^2 = 1$  [ $\Delta T_* = \Delta T_*(d_{\max})$ ].

The model relies on two different analyses depending on whether  $d$  is small ( $< d_{\min}$ ) or is large ( $> d_{\min}$ ). Hence, matching is required. For the sake of simplicity, we accept a nonanalytical matching at a chosen value of  $x = x_M$  defined by the condition

$$y_*(d \text{ small}, x = x_M) = y_*(d \text{ large}, x = x_M). \quad (26)$$

Matching is nonanalytic because derivatives  $dy_*/dx$  at  $x = x_M$  are not equal.  $x_M$  is chosen to be  $x_{\min} = d_{\min}/d_{\max}$  in which we recall that  $d_{\min}$  is the value of  $d$  at which  $\Delta T_*$  or  $P_*$  has a minimum. From Ref. 9 (see also Fig. 1), we have  $x_M = x_{\min} = 0.57$ . From relation (25), we conclude that  $\delta$  is indeed the natural matching constant needed to satisfy condition (26). We obtain  $\delta \approx 0.0264$ .

### F. Critical frequencies

When the steady state loses its stability to a time-dependent state, oscillations occur at a given basic fre-

quency  $f$  simply given by

$$f = \frac{1}{t_1 + t_2}. \quad (27)$$

Using  $t_1$  as a unit of time, dimensionless frequencies are

$$f^+ = ft_1 = \frac{t_1}{t_1 + t_2} = \frac{R}{R + 1}. \quad (28)$$

At marginality on BL1,  $R = R_* = \chi$ . Consequently, critical dimensionless frequency  $f_*^+$  is  $\chi/(\chi + 1)$ , i.e., critical frequencies  $f_*$  are

$$f_* = \frac{\chi}{(\chi + 1)t_{1*}}, \quad (29)$$

in which  $t_{1*}$  is the value of  $t_1$  on BL1.

For later comparisons with experiments, we again need a new dimensionless frequency variable that we define by using critical frequency  $f_*$  at  $d = d_{\max}$ :

$$z = f/f_*(d_{\max}). \quad (30)$$

Expressing  $t_1$  versus  $x$  and  $y$  for large  $d$ 's, then specifying that  $x$  and  $y$  are linked by (24) on BL1, and by using (29), we determine

$$f_*(d_{\max}) = \frac{\chi}{(\chi + 1)t_{1*}(d_{\max})} = \frac{\chi e^{2/3}}{(\chi + 1)K_1 C \gamma}, \quad (31)$$

in which  $C = |\Gamma|/(\alpha_T \rho_0 g K_T)$  contains thermophysical properties. It is then easy to establish that critical reduced frequencies  $z_*$  are given by

$$z_* = \begin{cases} \left[ \frac{3}{e} \right]^{1/3} \frac{\delta}{x^2}, & \text{small } d \\ \left[ \frac{y_*(x)^{1/3}}{x} \right]^2, & \text{large } d. \end{cases} \quad (32)$$

$$z_* = \begin{cases} \left[ \frac{3}{e} \right]^{1/3} \frac{\delta}{x^2}, & \text{small } d \\ \left[ \frac{y_*(x)^{1/3}}{x} \right]^2, & \text{large } d. \end{cases} \quad (33)$$

In (33),  $z_*$  is a double-valued function of  $x$  as  $y_*(x)$ . In establishing (32), constant  $\delta$  is first actually found to be  $K_1/k_1$ , i.e., a matching constant for frequencies. In practice, we did not find it useful to introduce a second matching constant and simply set  $K_1/k_1 = \delta$ . Again, we observe that the unknown  $\chi$  has disappeared and that (32) and (33) no longer contain thermophysical properties, thus providing again universal functions as confirmed by experiments.<sup>9,18</sup>

### G. A linear oscillator to model bifurcation on BL1

The above model agrees with experiments to describe the BL1 bifurcation (Sec. IV). To understand secondary instabilities inside BL1, the use of ODE's, i.e., of a dynamical system, is required. We first need a linear differential equation which must be equivalent to the described model. In writing this equation, we observe that we are interested in reduced critical quantities  $y_*/z_*$  [relations (23), (24), (32), and (33)] which do not contain the unknown quantity  $\chi$  any more, i.e., we may set  $\chi = 1$ .

We associate a mechanical oscillator with the free sur-

face and call  $\xi$  the deformation of the free surface above the heating source, the vertical axis oriented positively upwards. The linear equation of the mechanical oscillator may then be written as

$$\frac{d^2\xi}{dt^2} - \mu \frac{d\xi}{dt} + \omega^2\xi = 0, \quad (34)$$

with

$$\mu = \frac{1}{t_2} - \frac{1}{t_1} = \frac{R-1}{t_1}, \quad (35)$$

$$\omega = \frac{2\pi}{t_1 + t_2}. \quad (36)$$

In Eq. (34),  $\mu$  is a bifurcation control parameter. For  $\mu < 0$  ( $R < 1$ ), the system evolves to a fixed point. At  $\mu = 0$ , eigenvalues of (34) are a pair of conjugated complex numbers  $\lambda_{1,2} = (-\omega^2)^{1/2}$ . When  $\mu$  changes from negative to positive, the pair of eigenvalues of the stable focus for  $\mu < 0$  crosses the imaginary axis to produce an unstable focus, from which oscillations grow without any limit. The marginality condition is then  $\mu = 0$ , i.e.,  $R = 1$ , preserving our conclusions concerning critical  $y_*$ 's. Relation (36) ensures that the frequency of the system is  $1/(t_1 + t_2)$ , preserving also our conclusions concerning critical  $z_*$ 's.

With  $d$  as a unit of length and  $t_1$  as a unit of time, we introduce  $r = \xi/d$  and an overdot to designate dimensionless time derivation  $t_1/(d/dt)$ . Equation (34) then becomes

$$\ddot{r} - (R-1)\dot{r} + \left[ \frac{2\pi R}{R+1} \right]^2 r = 0, \quad (37)$$

which is equivalent to a one-parameter  $R(x, y)$  two-dimensional dynamical system in phase space  $(r, \dot{r}) = (y_1, y_2)$ .

#### H. A nonlinear oscillator (Hopf bifurcation)

Actually, nonlinearities must be added to (37) to prevent oscillatory motion to grow without any limit when  $R > 1$ . Due to a large degree of arbitrariness, we do not give extensive details but present our result as an ansatz:

$$\begin{aligned} \dot{y}_1 &= y_2, \\ \dot{y}_2 &= (R-1)y_2 - R^a(\sinh y_2 - y_2) - \left[ \frac{2\pi R}{R+1} \right]^2 \sinh y_1. \end{aligned} \quad (38)$$

We may check that the added nonlinear function  $f(y_1, y_2)$  tends to zero when  $y_1, y_2 \rightarrow 0$ . When instability occurs ( $R > 1$ ), the system evolves to an attracting limit cycle. At  $R = 1$ , the fixed point loses its stability through a supercritical Hopf bifurcation. Prefactor  $R^a$  accounts for the fact that we expect the nonlinear complementary damping term to depend on  $R$  as does the linear term. Exponent  $a$  could be taken as equal to 1 but has been actually adjusted to 1.4. This value leads to a matching of cycle limit amplitudes inside BL1 at  $x = x_M$  (Sec. III E) and  $y = 1.15$  which is the arithmetic mean value between

$y = 0$  and 2.3 (the largest  $y$  value considered in HBE's experiments<sup>9</sup>). The limit cycle amplitude is here defined as  $r_\infty = \lim_{t \rightarrow \infty} r_\Sigma$  in which  $r_\Sigma$  is the value of  $r$  in the Poincaré section  $\Sigma = \{r \in \mathbb{R}^+ | \dot{r} = 0\}$ .

#### I. The model for secondary instabilities

System (38) is basically a model for HWE's in which the temperature at the heating source is fixed. In the planar phase space  $(y_1, y_2)$ , nonwandering sets may only be fixed points, closed orbits, heteroclinic and homoclinic cycles (Ref. 1, Sec. 1.8), i.e., secondary instabilities observed in HBE's cannot be produced by this model. At first, we believed that this fact also explained the absence of secondary instabilities in HWE's because hot-wire temperature is controlled at a fixed value. Afterwards, we realized that the HWE's geometry is rather particular insofar as the hot-wire is a one-dimensional (1D) singular line embedded in a 3D fluid, and that, even if the temperature is fixed on this 1D line, it is allowed to change in a 3D neighborhood of it. Consequently, we could expect similar secondary instabilities both in HBE's and HWE's. More recent HWE's and interpretation (unpublished) showed that actually the range of  $y_*$ 's investigated in HWE's is too small to reach the domain of secondary instabilities. In both cases (HBE's and HWE's), the maximal value of investigated  $y_*$ 's was limited by phenomena such as boiling or production of bubbles. However, the spectroscopy cell used in HBE's was sealed while the HWE's were carried out at atmospheric pressure. Due to the increase of pressure in the sealed spectroscopy cell, higher  $y_*$ 's would be allowed in HBE's than in HWE's. More experiments are planned to check the validity of this discussion.

In any case, to produce a model with secondary instabilities as observed in HBE's we must increase the dimension of phase space. The new dimension is 3 by adding a new variable linked to temperature at the heating source which is not fixed any more. This variable  $s = y_3$  must be dimensionless and is defined by

$$s = \frac{T - T_{st}}{T_{st} - T_a}, \quad (39)$$

in which  $T_{st}$  is the steady temperature in the absence of instability,  $T_a$  the ambient temperature above the free surface, and  $T$  the actual time-dependent temperature.  $s$  ranges from 0 (steady case) to  $-1$  ( $T = T_a$ , maximal cooling by Marangoni convective flow).

The steady temperature difference  $\Delta T = T_{st} - T_a$  must be replaced by a time-dependent temperature difference  $\Delta T' = T - T_a$ , which is also, from (39),  $\Delta T(1+s)$ . For  $d$  small,  $R$  is proportional to  $\Delta T d$  [relation (11)]. For large  $d$ , it is proportional to  $\Delta T^{1/3}$  with also an exponential term containing  $d^3 \Delta T$  which further decreases the value of  $R$  [relation (12)]. Hence correction  $(1+s)$  intervenes as  $1+s$  for  $d$  small but only as  $(1+s)^{1/3}$  with exponential correction for  $d$  large. We may consequently expect that secondary instabilities are more likely to occur for small  $d$  than for large  $d$ . As a matter of fact, the structure of  $R$  for large  $d$  even limits the occurrence of the primary in-

stability (Hopf bifurcation) since for  $d > d_{\max}$ , the system is always steady. When  $d$  is large, the distance between the free surface and the heating source leads to the existence of a screening effect. These remarks are in agreement with experiments because secondary instabilities have only been observed for  $d$  small. Then, only this case is now discussed.

When oscillations of the free surface occur in HBE's, distance  $d$  becomes  $d(1+r)$  and temperature difference becomes  $\Delta T(1+s)$ . Since  $R \simeq \Delta t d$ , the new mechanical oscillator is simply deduced from the old one in (38) by changing  $R$  to

$$R' = R(1+r)(1+s). \quad (40)$$

It remains to model a third equation  $\dot{y}_3 = f_3(r, \dot{r}, s)$  for what we shall call, perhaps improperly, a thermal oscillator. This is the most difficult task in which some arbitrariness will be again introduced. We start from the temperature equation

$$\frac{\partial T}{\partial t} + U_j \frac{\partial T}{\partial x_j} = K_T \frac{\partial^2 T}{\partial x_j^2} + S, \quad (41)$$

with classical notations,  $S$  being the laser heating source term. We note that no source term  $S$  appeared in the previous model in 2D phase space because it was expressed in terms of  $\Delta T / \Delta T_*(d_{\max})$  or  $P / P_*(d_{\max})$ . The explicit introduction of  $S$  is, however, now required. We also remark that the heat transfer to the liquid in HWE's is expected to depend on fluid velocity while in HBE's there is a constant heat production in the liquid when the system is steady. For such a steady state ( $\partial T / \partial t = 0$ ), with  $d$  small (convection neglected,  $t_1$  is a diffusion time), we may evaluate source  $S$  by

$$S = -K_T \frac{\partial^2 T}{\partial x_j^2} \simeq K_T \frac{T_{\text{st}} - T_a}{d^2}. \quad (42)$$

In the oscillating case inside BL1, the convection term must be preserved due to the cooling Marangoni convection and the source term must be modified because modifications of temperature  $T$  associated with modifications of temperature gradients  $\partial T / \partial x_j$  influence the focus of the laser beam (thermal lens effect). The source term consequently becomes time-dependent:

$$S' = H(t)S. \quad (43)$$

Equation (41) may be rewritten as

$$\frac{\partial T}{\partial t} + \mathcal{C}_1 = K_T \frac{\partial^2 T}{\partial x_j^2} + H(t)S, \quad (44)$$

where  $\mathcal{C}_1$  is a convection term. The diffusion term in (44) may be evaluated as

$$-K_T \frac{T - T_a}{d^2(1+r)^2}, \quad (45)$$

in which the appropriate length scale is now  $d(1+r)$  instead of  $d$ .

From (44), (45), and (42), we obtain

$$\frac{\partial T}{\partial t} = \frac{K_T}{d^2} \left[ H(t)(T_{\text{st}} - T_a) - \frac{T - T_a}{(1+r)^2} \right] - \mathcal{C}_1. \quad (46)$$

Introducing in (46) the definition (39) of  $s$ , and taking  $t_1 = d^2 / K_T$  as a unit of time to express the dimensionless time derivative (overdot), (46) is translated into

$$\dot{s} = \left[ H(t) - \frac{1+s}{(1+r)^2} \right] - \mathcal{C}_2. \quad (47)$$

The evolution (47) of the thermal oscillator is then controlled by a net source term (laser heating minus diffusion loss) and a cooling Marangoni convection term. To model the convection term  $\mathcal{C}_2$ , we note that it must have the form [see convection term in (41)]

$$\mathcal{C}_2 = \frac{\epsilon f(s)}{\mathcal{L}}, \quad (48)$$

in which  $\epsilon$  is a dimensionless velocity scale (associated with  $U_j$ ),  $\mathcal{L}$  a dimensionless length scale (associated with derivative with respect to  $x_j$ ), and  $f(s)$  a dimensionless function of  $s$  (associated with quantity  $T$  to be derived).

For  $\epsilon$ , we own two relevant scales. The first one is the dimensionless Marangoni velocity  $V_M^+ = R$  [relation (11) with  $k_1/k_2 = 1$ ] representing a constant overall convection velocity due to drag exerted by the free surface on the underlying liquid. It must be modulated by a second time-dependent velocity which is simply the free surface velocity  $\dot{r}$ . A good candidate is then

$$\epsilon = (|R - 1| |\dot{r}|)^{1/2}. \quad (49)$$

Further justifications for this proposal are as follows. If  $|R - 1|$  and  $|\dot{r}|$  were made dimensional again, (49) would ensure that  $\epsilon$  is a velocity, not (for instance) the square of velocity.  $R - 1$  is used rather than  $R$  to better ensure that scale  $\epsilon$  decreases to zero when we approach Hopf bifurcation on BL1. The choice of modulus  $|R - 1|$  instead of  $R - 1$  enables us to observe the approach to the fixed point when  $R < 1$ . Finally, introduction of  $|\dot{r}|$  instead of  $\dot{r}$  produces a real positive  $\epsilon$  in agreement with the fact that the liquid is driven upward by Marangoni effect.

To model  $f(s)$ , we rely on a picture of convection obtained from numerical integration of the full PDE's (Ref. 20) (which is, however, in agreement with a common sense of physics). Streamlines leave the heating source to move upward, split to a double eddy when approaching the surface, and return to the heating source location from below. Cooling occurs along streamlines and the fluid returning to the heating source is cold. Hot fluid at the heating source being very efficiently swept by convection and replaced by cold fluid at temperature  $\simeq T_a$  ( $s \simeq -1$ ),  $|\Delta s|$  on the streamline is of the order of 1 when  $T$  is about  $T_{\text{st}}$ . Conversely, when efficient cooling has occurred and  $T \simeq T_a$ , i.e.,  $s \simeq -1$ , further cooling is inefficient because it mainly results from heat diffusion. This discussion suggests that we may propose

$$f(s) = 1 + s^m, \quad (50)$$

in which  $m$  must be odd to ensure  $f(s) < \max|\Delta s| = 1$  and

very large to ensure efficient cooling except when  $s$  approaches  $-1$ . In practice,  $m$  has been set equal to 5001, essentially providing a sharp cutoff. The precise value is not essential. When  $m$  decreases, we simply numerically observe that the richness of secondary instabilities progressively disappears. When  $s=0$  ( $T=T_{st}$ ),  $f(s)=1$  and cooling convection is the most efficient. Even for  $s=-0.999$ , this efficiency is only decreased by less than 1%. Finally, for  $s=-1$  ( $T=T_a$ ), no cooling occurs at all.

For scale length  $\mathcal{L}$ , our qualitative picture of convection leads to  $\mathcal{L} \simeq 1$  with  $d$  as a unit of length, completing the modeling of  $\mathcal{C}_2$  [relation (48)].

We still have to discuss  $H(t)$  in relation (47). We found the task of modeling  $H(t)$  rather difficult. In this paper, we shall be content with a very approximate solution to this problem. We note that we expect  $H=H(y)$  since focus and loss of focus effects are expected to depend on laser power and also  $H > 1$  due to a better focus when  $s$  decreases. Neglecting the fact that  $\partial H / \partial t \neq 0$ , the above remarks are approximately satisfied if we abruptly propose to replace the source term of (47) by

$$\left[ 1 - \frac{1+s}{(1+r)^2} \right] y^{0.70}, \tag{51}$$

in which again the exact value 0.70 of the exponent is not critical. It simply controls the location of fatal bifurcations in the control plane (see Sec. IV F).

Assembling all the results of this subsection, we obtain the following two-parameters  $(R, y)$  three-dimensional dynamical system in phase space  $(r, \dot{r}, s) = (y_1, y_2, y_3)$ :

$$\begin{aligned} \dot{y}_1 &= y_2, \\ \dot{y}_2 &= (R' - 1)y_2 - R'^{1.40}(\sinh y_2 - y_2) - \left[ \frac{2\pi R'}{R' + 1} \right]^2 \sinh y_1, \\ \dot{y}_3 &= \left[ 1 - \frac{1+y_3}{(1+y_1)^2} \right] y_3^{0.70} - \sqrt{|R-1|} |y_2| (1+y_3^{5001}), \end{aligned} \tag{52}$$

in which  $R'$  is given by relation (40).

#### IV. MODEL RESULTS AND COMPARISONS WITH EXPERIMENTS

##### A. Critical $y_*$ 's for Hopf bifurcation

We refer to HBE's.<sup>9,15</sup> In this case, the meaning of  $y_*$  is  $P_*/P_*(d_{max})$ . Experimental values for  $d_{max}$ ,  $P_*(d_{max})$  are 2.72 mm and 173 mW, respectively (see Fig. 1). Results from Refs. 9 and 15 expressed as  $P_*(d)$  are then reexpressed as  $y_*(x)$ . Theoretical values are obtained from (23) and (24). Comparisons between experimental and theoretical values are shown in Fig. 3. Agreement is very satisfactory.

Furthermore, having shown in Ref. 9 that experimental data for HBE's and for HWE's with oil labeled 47V5 are similar and in Ref. 18 that all data for HWE's, whatever the oil, are also similar, it follows that the model correctly explains both HBE's and HWE's simultaneously.

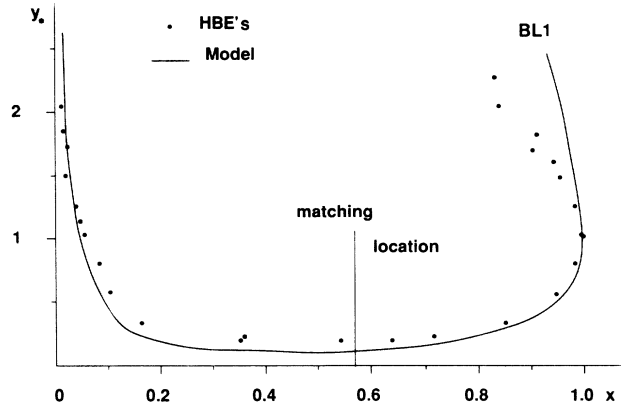


FIG. 3. Critical thermal constraints  $y_*$  vs reduced distance  $x$  for Hopf bifurcation. Comparisons between model and HBE's.

##### B. Critical $z_*$ 's for Hopf bifurcation

Similarly, experimental results from Refs. 9 and 15 are reexpressed as  $z_*(x)$  with  $f_*(d_{max})=0.51$  Hz. Theoretical values are obtained from (32) and (33),  $y_*$ 's in (33) being previously computed from (23). Comparisons are shown in Fig. 4 and found again to be very satisfactory. Agreement with HWE's would also be satisfactory due to similarity between HBE's and HWE's.<sup>9,18</sup>

##### C. Oscillation amplitudes inside BL1

Neglecting secondary instabilities inside BL1, this subsection and the next one examine whether nonlinear dynamical system (38) correctly reproduces experimental data concerning oscillation amplitudes and frequencies inside BL1, in order to test whether our proposal for nonlinearities is acceptable.

Measurements in HBE's have been carried out for several  $P$ 's, from 34 to 400 mW. To limit the number of

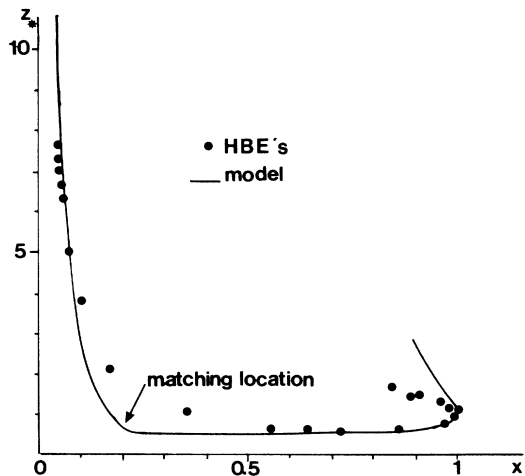


FIG. 4. Critical reduced frequencies  $z_*$  vs reduced distance  $x$  for Hopf bifurcation. Comparisons between model and HBE's.

figures, we only discuss measurements for  $P=140$  mW,<sup>9,15</sup> i.e.,  $y=0.8092$ . For this value, we compute  $R$  for  $d$  small and  $d$  large according to readily established formulas:

$$R = \begin{cases} \chi \left[ \frac{k_1}{k_2} \right]^2 \frac{1}{\delta} \left[ \frac{e}{9} \right]^{1/3} xy, & \text{small } d \\ \chi \frac{(ey)^{1/3}}{x} \exp(-\frac{1}{3}yx^3), & \text{large } d \end{cases} \quad (53)$$

in which we specify  $\chi=1$  (Sec. III G). Also, computing  $R_*$  from (53) by using (23), we find that  $(k_1/k_2)^2=1$ , i.e., the unknown constants  $k_1, k_2$  disappear from (53).

With the obtained  $R$  values, (38) is integrated by using a fourth-order Runge-Kutta algorithm and limit cycle amplitudes are measured by  $r_\infty$  in Poincaré section  $\Sigma = \{r \in \mathbb{R}^+ | \dot{r} = 0\}$ , see Sec. III H. We call  $r_\infty^d$  and  $r_\infty^D$ ,  $r_\infty$  values obtained for small  $d$  and large  $d$ , respectively. Matching in nonlinear domain inside BL1 is defined by considering the natural average:

$$\bar{r}_\infty = r_\infty^d (1-x) + r_\infty^D x. \quad (55)$$

Results are shown in Fig. 5 exemplifying the good quality of matching in nonlinear domain generated by exponent  $a=1.4$  in (38) and averaging process (55). To compare with experimental data, we use  $\bar{r}_\infty$  (a free surface deformation). Comparison cannot, however, be direct because free surface deformations could not be measured. The amplitudes of oscillations were measured through amplitudes  $A_{dB}$  of the fundamental frequency in Fourier Transform spectra of signals obtained by tracking variations of laser light intensities beyond the cell. It makes sense to compare  $\bar{r}_\infty$  (actually  $r_{\infty dB} = 10 \log_{10} \bar{r}_\infty$ ) and  $A_{dB}$  because oscillations of the laser beam originate

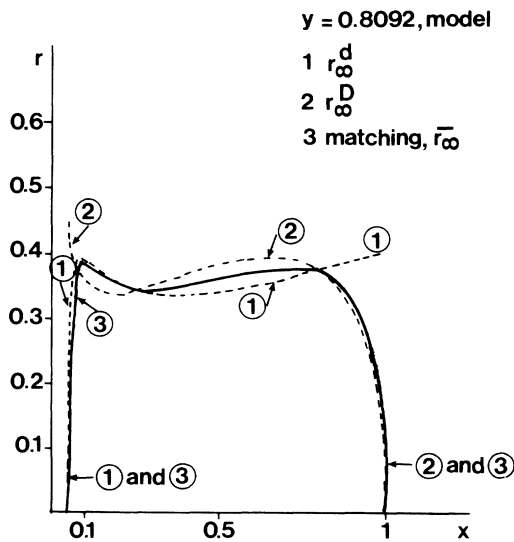


FIG. 5. Amplitudes of limit cycles inside CT1 for 2D dynamical system. There is matching between domains “ $x$  small” and “ $x$  large.”

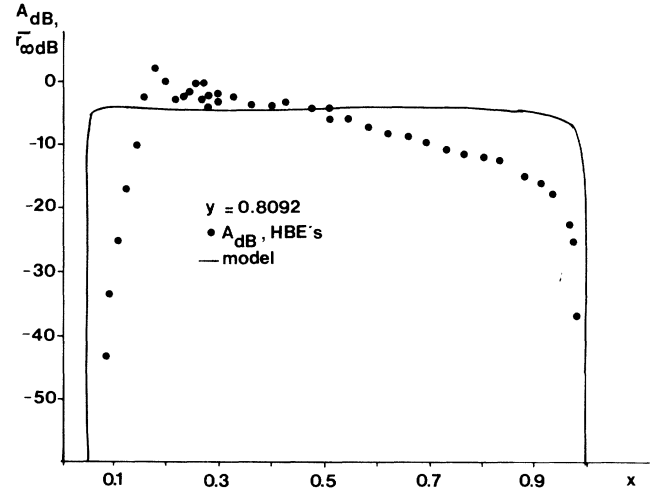


FIG. 6. Amplitudes of limit cycles inside CT1. Comparisons between model (2D dynamical system) and HBE's.

from oscillations in the fluid which are strongly correlated with free surface oscillations. After applying a drift of 30.46 dB to experimental  $A_{dB}$ , the comparison is displayed in Fig. 6. The similarity between model and experiments is striking. In both cases, increase and decrease of oscillations near the frontiers of the Hopf bifurcation are very abrupt, with a rather flat plateau in between.

#### D. Frequencies inside CT1

Integrating (38), we also obtain  $T_\infty = \lim_{t \rightarrow \infty} T$  in which  $T$  is the dimensionless return time to Poincaré section  $\Sigma$ . With variable  $z$  defined in Sec. III F, relation (30), we readily show that theoretical  $z$ 's are given by

$$z_d = \begin{cases} \frac{\chi+1}{\chi} \frac{K_1}{k_1} \left[ \frac{3}{e} \right]^{1/3} \frac{1}{T_\infty x^2}, & \text{small } d \\ \frac{\chi+1}{\chi} \left[ \frac{y}{e} \right]^{1/3} \frac{\exp(\frac{1}{3}yx^3)}{T_\infty x}, & \text{large } d \end{cases} \quad (56)$$

in which we also specify  $\chi=1$  and recall that  $K_1/k_1$  is the matching constant  $\delta$ . We may again define a matched  $\bar{z}$  by

$$\bar{z} = z_d(1-x) + z_D x. \quad (58)$$

Experimental data in Ref. 9 are reexpressed as  $z(x)$  and comparisons are shown in Fig. 7. Agreement between experimental data and matched  $\bar{z}$ 's is very good. The modifications introduced by secondary instabilities (SI), not introduced here in model results, are indicated on experimental data.

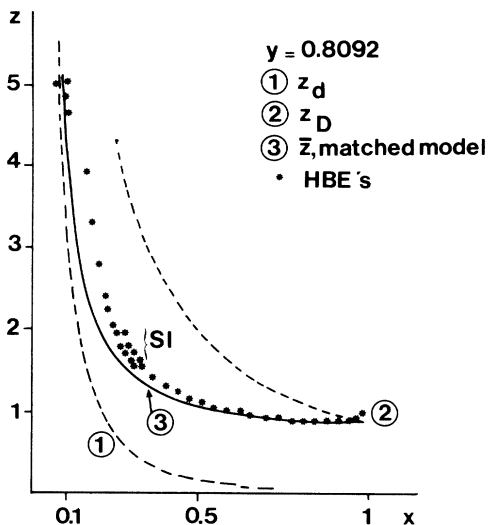


FIG. 7. Reduced frequencies vs reduced distance inside CT1 for 2D dynamical system. Matching between domains “x small” and “x large.” Comparisons between model and HBE’s.

E. State diagram for the 3D dynamical system

The 3D dynamical system (52) is integrated by using a fourth-order Runge-Kutta algorithm again. The state of the system is determined by examining an asymptotic sequence of  $s_\Sigma$  in which  $s_\Sigma$  is the value of  $s$  in a Poincaré section  $\Sigma = \{\dot{r} \in \mathbb{R}^-, s \in [0, -1] | r = 0\}$  and/or by carrying out a discrete FFT on this sequence. The model state diagram is displayed in Fig. 8 (restricted to small  $x$ ) in

which BL1 (model) is also reported.

After BL1, we successively encounter curves BL2, BL3, BL4, . . . , each one corresponding to a period doubling of limit cycles (notation  $p_i$  designates a signal of period  $i$  in  $\Sigma$ ), leading eventually to three chaotic domains, presumably after infinite Feigenbaum subharmonic cascades. Points labeled  $C$  designate chaotic signals characterized by a noisy continuous background in FFT spectra, on which some periodic peaks may possibly still remain visible corresponding to inverse cascades and band chaos as in unimodal maps.<sup>2</sup> Points labeled  $P_3, P_6, P_{10}, P_{12}$  indicate the existence of periodic windows. Intermittency can also be observed in chaotic domains. Figures 9 and 10 show two examples of what appears numerically to be strange chaotic attractors, the first one for  $x=0.2, y=2.0$  in the rightmost chaotic domain, the second one for  $x=0.16, y=1.4$  in the bottom chaotic domain. We also observe a line FB of fatal bifurcations discussed below.

F. Fatal bifurcations

When the deformation of the free surface becomes too large [ $y(1) < -1$ ],  $R'$  in (52) becomes negative and the system is no longer definite due to the factor  $R'^{1.40}$ . This corresponds to a violent motion of the surface which would be bent down to expose the heat source in air. We call such an event “fatal.”

Relying on numerical computations, we found that inside a line FB fatal events are sure to occur. We state that the asymptotic state of the system is non definite with an infinite basin of attraction. Outside FB, two

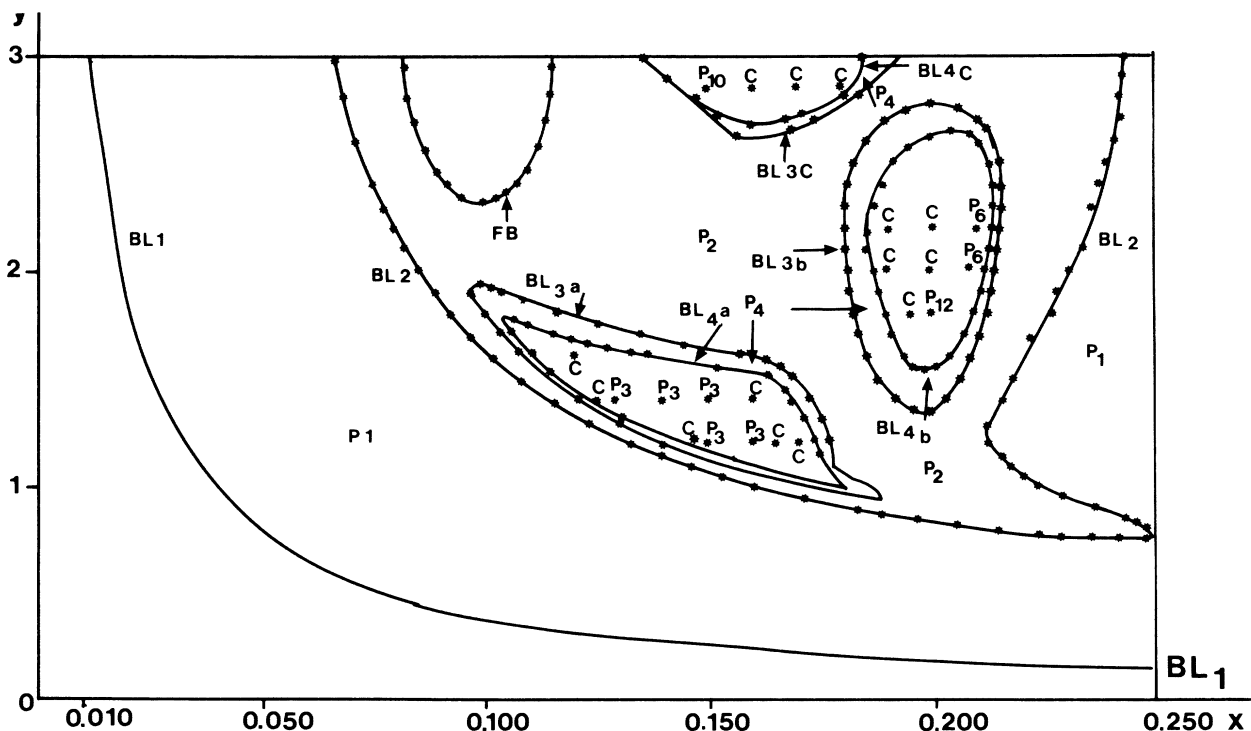


FIG. 8. State diagram for the two-control  $(x, y)$  3D model.

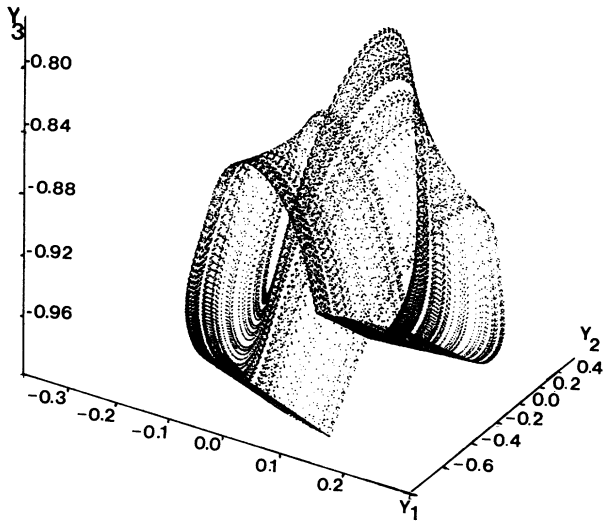


FIG. 9. A (presumably) strange chaotic attractor.  $x=0.2$ ,  $y=2.0$ .

asymptotic states are possible, definite or nondefinite, depending on initial conditions. The basin of attraction of the definite state is not infinite. When we approach line FB from outside, the basin of attraction of the definite state shrinks to zero and disappears on FB.

Approaching FB, we observe in Fig. 8 that definite asymptotic states are of the kind  $p_2$  in  $\Sigma$ , with return times  $T_1$  and  $T_2$  ( $T_1 < T_2$ ). Due to shrinking of the definite state basin of attraction, the approach to FB is studied by an adiabatic marching procedure, i.e., we fixed  $x$  and increased  $y$ , initial conditions for the  $n$ th run being asymptotic conditions of the  $(n-1)$ th run.  $T_1$  is essentially unaffected when approaching FB while  $T_2$  seemingly tends towards infinity, faster than  $\exp(y)$ , leading to unaffordable CPU's to locate the critical  $y_{FB}$ 's of fatal bifurcations. Critical  $y_{FB}$ 's are then evaluated by extrapo-

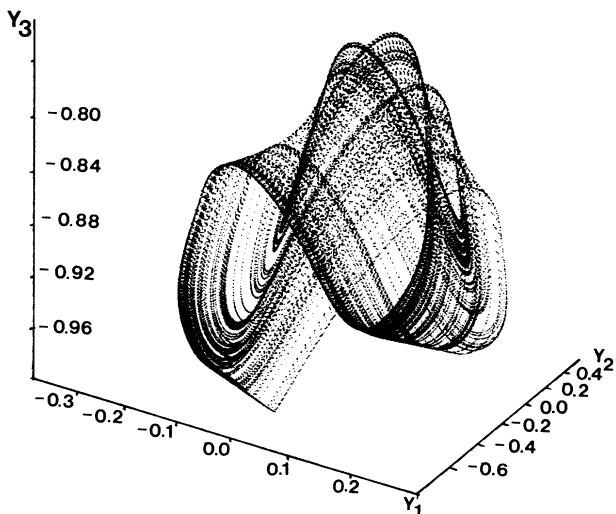


FIG. 10. Another strange chaotic attractor.  $x=0.16$ ,  $y=1.4$ .

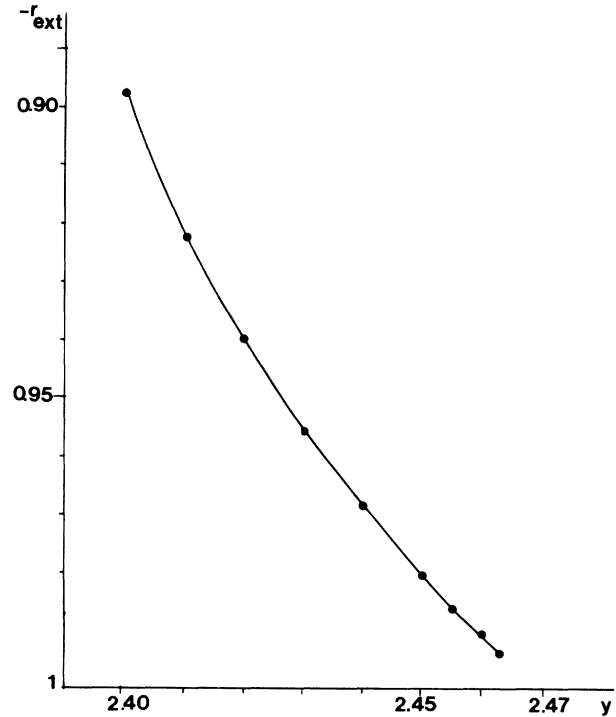


FIG. 11.  $r_{\text{ext}}$  vs  $y$  for  $x=0.09$ . Approach to a fatal bifurcation.

lating  $r_{\text{ext}}(y)$  to  $r_{\text{ext}} = -1$ ,  $r_{\text{ext}}$  being  $\min(y_1)$  during a run. An example is given for  $x=0.09$  in Fig. 11 leading to  $y_{FB} \approx 2.47$ .

### G. Stewart's program

Stewart's program<sup>27</sup> defines criteria for comparing the asymptotic behavior of a true system (here experimental HBE's and HWE's) with its model. Most of this program has been completed in this paper. Both the true system and its model have a steady state separated from oscillation states by a supercritical Hopf bifurcation. This bifurcation is described in a 2D phase space required for Hopf bifurcation in normal form<sup>2</sup> with two control parameters  $(x, y)$  which are actually absorbed in a single one  $R$ .

The Hopf bifurcations in the true system and its model agree not only qualitatively but also quantitatively, as shown in Figs. 3 and 4 and in Figs. 6 and 7. For secondary instabilities, the model is a 3D dynamical system with two parameters  $(x, y)$  which explains why they only occur for small  $d$ . Comparison between Figs. 1 and 8 shows a fair degree of resemblance between the model and the true system. Even something similar to fatal bifurcations is observed in the true system. In the model, fatal bifurcations occur when the laser power increases by producing too much violent motion of the free surface. In the true system they occur, for instance, because the increase of laser power leads to liquid boiling, destroying the system under study and limiting experiments when  $y$  increases. All these positive results have been obtained with a remarkable economy of physical and mathemati-

cal tools, particularly when we consider the complexity of the true system defined by intricate coupled nonlinear PDE's with a high lack of symmetry.

Clearly, a model is not a simulation and we do not really believe that all the model ingredients will resist future experiments and developments. However, we have certainly reached a fair understanding of experimental phenomena, much better than what has been hitherto possible. The most significant disagreement between Figs. 1 and 8 is due to the fact that the model fails to predict quasiperiodicity and associated hysteresis. Several lines of research may be proposed to improve the model and reduce this disagreement. A first one concerns our poor modeling of  $H(t)$  in which we assumed  $\partial H/\partial t=0$ . Qualitatively, if we satisfied  $\partial H/\partial t \neq 0$ , we should have to introduce a characteristic time of thermal oscillator associated with relaxation in focusing and defocusing of laser beam when  $s$  evolves. Quasiperiodicity might then result from the interplay between this relaxation time and the period of the mechanical oscillator. Another possibility is that the local system of mechanical and thermal oscillators could be forced by propagating waves reflected by cell walls and therefore returning to the space domain where they have been generated. Dynamical system (52) would then become a nonautonomous system equivalent to an autonomous one in  $\mathbb{R}^4$ . A last idea might be to introduce a hydrodynamic oscillator coupling with the oscillators of (52). The existence of such a hydrodynamic oscillator is reported by Bazhenov *et al.*,<sup>28</sup> who observed in several cases a periodic creation of vortices near the main jet of flow. Phase space would then become  $\mathbb{R}^6$ . These questions open the way to more research in model developments and also in experiments.

Although chaos is not observed in Fig. 1, HBE's may evolve towards it (Ref. 8 and unpublished experiments). Besides qualitative observation that both the true system and its model produce chaos, Stewart's program leads us to ask how chaos of the true system and its model compares quantitatively. For the sake of later comparison with planned experiments, Sec. V is devoted to metric and dynamical characterization of the attractor displayed in Fig. 9. Another interest is the study of system (52) in its own right.

## V. CHARACTERIZATION OF A STRANGE CHAOTIC ATTRACTOR

### A. Generalities

We now consider the object depicted in Fig. 9. Although Lyapunov exponents have not been quantitatively determined, we rely on the existence of a noisy background in frequency domain and on sensitivity to initial conditions in time domain to state that this object numerically behaves as a strange chaotic attractor.

Among a host of quantities used to characterize such attractors, we may select generalized dimensions  $D_q$  and entropies  $K_q$  defined as follows.<sup>29-34</sup> Attractor  $A$  is partitioned into boxes of size  $l$  numbered from 1 to  $M(l)$ . The probability measure of box  $i$  is  $p_i$ . Generalized dimensions  $D_q$  are given by

$$D_q = \frac{1}{q-1} \lim_{l \rightarrow 0} \left[ \ln \sum_{i=1}^{M(l)} p_i^q / \ln l \right]. \quad (59)$$

Next, we consider the probability  $p(i_1, i_2, \dots, i_b)$  of finding the system in box  $i_1$  at time  $t$ ,  $i_2$  at time  $t + \Delta t, \dots, i_b$  at time  $t + (b-1)\Delta t$ . Generalized entropies  $K_q$  (or order- $q$  Kolmogorov entropies) are given by

$$K_q = \sup_{B, \Delta t} \left[ \lim_{b \rightarrow \infty} \frac{1}{1-q} \frac{\ln \sum_{i_1, i_2, \dots, i_b} p(i_1, \dots, i_b)^q}{b \Delta t} \right], \quad (60)$$

in which  $B$  designates a partition. Furthermore, one proves that

$$D_q \geq D_p, \quad K_q \geq K_p, \quad p > q. \quad (61)$$

Box-counting algorithms are inefficient when the fractal dimensions become higher than 2 or 3 (Ref. 35). Furthermore, in experiments, the true attractor  $A$  of the dynamical system is generally not accessible. The original attractor  $A$  may then be projected into  $\mathbb{R}^n$  to provide a reconstructed attractor  $A^p$  having the same  $D_q$ 's,  $K_q$ 's, for instance, by using the time-delay method.<sup>36-38</sup> Generalized quantities may then be determined (on  $A$  or  $A^p$ ) by a fixed-radius approach to be recommended for  $q > 1$ , a fixed-mass approach to be recommended for  $q < 1$  (ref. 39) or from the knowledge of unstable periodic orbits which are dense in the attractor.<sup>40-43</sup> Fixed-mass (and/or  $k$ th nearest-neighbor method) is discussed in Refs. 44-47. In this paper, we use a fixed-radius method with a Grassberger-Procaccia-type algorithm as discussed in Refs. 48-53.

Once  $D_q$ 's and  $K_q$ 's are determined (and smoothed), Legendre transforms enable us to determine singularity spectra  $f_D(\alpha_D)$  and  $f_K(\alpha_K)$ , respectively,<sup>54,55</sup>

$$\begin{aligned} \alpha_X(q) &= \frac{d}{dq} [(q-1)X_q], \\ f_X(d_X(q)) &= q\alpha_X(q) - (q-1)X_q, \\ X &= D, K, \end{aligned} \quad (62)$$

with, however, warning that the required smoothing of  $X_q$  may prevent the detection of phase-transition-like critical points for nonhyperbolic attractors.<sup>56,57</sup>

### B. A Grassberger-Procaccia-type algorithm

The reconstructed attractor is produced as follows. We consider a temporal signal  $X(t)$  sampled at times  $(t+i\Delta t)$ ,  $i$  integer, and build a vectorial temporal sequence  $\mathbf{X}(i\Delta t) = \mathbf{X}(i)$  in  $\mathbb{R}^n$ . The components of vector  $\mathbf{X}(i)$  are  $(X(i), X(i-p), \dots, X(i-(n-1)p))$ , in which a discrete time  $j$  is meant for a time  $j\Delta t$ .  $i$  and  $p$  are the discrete time and the discrete time delay, respectively.

We define a local correlation  $C_i(l)$  at point  $\mathbf{X}(i)$  by the relation

$$C_i(l) = \frac{1}{N-1} nb \{j \neq i, \|\mathbf{X}(i) - \mathbf{X}(j)\| \leq l\}, \quad (63)$$

in which  $j$  ranges from 1 to  $N$ ,  $N$  being the size of the

temporal sequence (the number of vectors in it).  $\| \cdot \|$  is a norm to compute the distance between vectors  $\mathbf{X}(i)$  and  $\mathbf{X}(j)$ . In this work, we use the  $\infty$  norm (maximum among the absolute values of the component differences).

Spatially averaging local correlation moments, we define the order- $q$  correlations  $C_q(l)$  as

$$C_q(l) = \frac{1}{m} \sum_{i=1}^m C_i^{q-1}(l), \quad q \neq 1. \quad (64)$$

For  $q=1$ , we define the order-1 correlation  $C_1(l)$  as

$$C_1(l) = \left[ \prod_{i=1}^m C_i(l) \right]^{1/m}. \quad (65)$$

Assuming that the measure is ergodic on the attractor, we then show that<sup>58-60</sup>

$$\lim_{l \rightarrow 0} C_q(l) \simeq r^{QD_q}, \quad (66)$$

in which  $Q$  is  $q-1$  for  $q \neq 1$  and 1 for  $q=1$ . In practice, size  $N$  of the temporal sequence and number  $m$  of central vectors are finite (with preferably  $m \ll N$ ) preventing the reaching of the limit  $l \rightarrow 0$  in (66). This scaling relation is then only observed in a finite domain ( $l_{\min}, l_{\max}$ ) of  $l$ . Correlations  $C_q$  are evaluated at discrete values  $l_i$  of  $l$  in ( $l_{\min}, l_{\max}$ ), separated by equal distances in logarithmic scales. Local slopes  $D_q(l_i)$  are computed and averaged to evaluate  $D_q$ . An insight on the accuracy of the results is obtained from the standard mean deviation  $\sigma_D$  of local slope values, although this value of  $\sigma_D$  must not be taken too seriously due, for instance, to lacunarity effects.<sup>61</sup>

The algorithm to evaluate  $D_q$ 's on the original attractor  $A$  is similar but for the fact that the trajectory vector  $\mathbf{X}(i)$  must now be the trajectory vector in the original phase space [here  $y_i(t)$ , relation (52)].

Evaluation of  $K_q$ 's is obtained by computing correlation  $C_q$ 's in phase spaces of increasing dimensions in scaling domains ( $l_{\min}, l_{\max}$ ). Noting  $C_q^n$  for  $C_q$  computed in  $\mathbb{R}^n$ , we define

$$K_q^n = \frac{1}{ps \Delta t} \ln [C_q^n(l) / C_q^{n+s}(l)], \quad (67)$$

in which  $s$  is an increment in phase-space dimension.  $K_q$ 's are then evaluated as

$$\lim_{n \rightarrow \infty} K_q^n = QK_q. \quad (68)$$

In practice, finite resolution ( $N, m$ ) prevents the reaching of the limit  $n \rightarrow \infty$ .  $K_q^n / Q$  are then averaged on a plateau of  $K_q^n / Q$  for  $n$  in  $[n_{\min}, n_{\max}]$  to evaluate  $K_q$ 's, with an insight on accuracy provided by a standard mean deviation  $\sigma_K$ . These algorithms are implemented in computer programs.

### C. Metric properties of a HBE attractor

The attractor  $A$  of Fig. 9 is reconstructed in  $\mathbb{R}^n$  by using  $X = y_1, y_2$ , and  $y_3$  successively. Sophisticated procedures may be used to provide the best reconstruction<sup>62,63</sup> (singular value decomposition, redundancy

analysis). In our work, we use a simple pragmatic approach relying on the observation that the value of the window length  $(n-1)p\Delta t$  is the determinant parameter for the quality of the reconstruction.<sup>53</sup> We choose reasonable values for  $p$  and  $\Delta t$ , namely,  $\Delta t = 0.01$  providing about 250 sampling points per pseudoperiod  $T_0 \simeq 2.5$  [remember that time in (52) is dimensionless], and  $p=6$  corresponding to a temporal distance  $p\Delta t$  of about  $T_0/40$  between two successive components of reconstructed trajectory vectors. These values and the procedure under discussion have been tested in the case of the Lorentz attractor, leading to perfect agreement with data in the literature. To determine the window length, we are now left with the determination of an optimal value of  $n$ . Figure 12 shows local slopes  $D_2(l)$  with variable  $y_3$  for various  $n$ , computations being carried out with a small resolution  $(N, m) = (50\,000, 200)$ . We choose to display  $D_2$  because this dimension (the so-called correlation dimension) is maybe the most typical (and employed). Only some curves are provided but computations have been carried out by steps  $\Delta n = 5$  from  $n=5$  to 100. With  $D_2 \simeq 2$  (see below), the so-called Takens criterion states that  $n$  must be at least  $\simeq 2D_2 + 1 \simeq 5$ . For  $n=5$ , Fig. 12 shows that the reconstruction is poor. For  $n=10$ , we observe a scaling domain of high quality but dimensions are severely underestimated. Conversely, for  $n$  large the scaling domain dramatically deteriorates. An optimal  $n$  is  $n_0 = 25$ . For this value, however,  $D_2$  is smaller than 2, a fact which will require a specific discussion below, but note nevertheless that such a value  $D_2 < 2$  is also obtained when  $D_q$ 's are computed directly in  $\mathbb{R}^3$ , without any reconstruction (see Table I). We also checked that the optimal  $n_0 = 25$  is essentially insensitive to  $q$ .

$D_q$ 's are then computed in  $\mathbb{R}^{25}$  for  $y_1, y_2, y_3$  with  $(N, m) = (10^5, 2000)$  and also in  $\mathbb{R}^3$  on the original attractor of Fig. 9. Ideally, the chosen values for ( $l_{\min}, l_{\max}$ ) should be given. They are not reproduced in order to avoid overloading the paper with tables but a feeling of scaling domain quality may be gained from  $\sigma_D$  (Table I). It suffices to add that values of  $D_q$ 's are reasonably in-

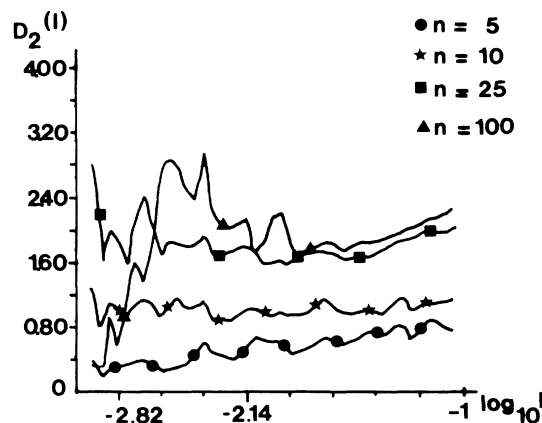


FIG. 12. Local slopes  $D_2(l)$  for reconstructed attractor in  $\mathbb{R}^n$  for several  $n$ 's. Determination of an optimal  $n$ . Symbols are used only to identify curves.

TABLE I.  $D_q$  vs  $q$ , evaluated in  $\mathbb{R}^3$ , and in  $\mathbb{R}^{25}$  with  $y_1, y_2, y_3$ . Columns 1–4 have resolution  $(10^5, 2000)$ . Column 5 has  $(2 \times 10^6, 2000)$ .  $D_q$  are given with more digits than allowed by  $\sigma_D$  because  $\sigma_D$  is a poor representative of actual accuracy. In columns 2–4  $\epsilon$  refer to  $D_q$ 's in column 1. In column 5,  $\epsilon$  refers to column 2.

$q$	1		2			3			4			5		
	$D_q$ in $\mathbb{R}^3$		$D_q$ in $\mathbb{R}^{25}$			$D_q$ in $\mathbb{R}^{25}$			$D_q$ in $\mathbb{R}^{25}$			$D_q$ in $\mathbb{R}^{25}$		
	$D_q$	$\sigma_D$	$y_1$	$\sigma_D$	$\epsilon$ (%)	$y_2$	$\sigma_D$	$\epsilon$ (%)	$y_3$	$\sigma_D$	$\epsilon$ (%)	$y_1$	$\sigma_D$	$\epsilon$ (%)
-25	2.36	0.4	2.11	0.4	11	2.36	0.2	0	2.35	0.4	0.4	2.07	0.3	2
-10	2.40	0.3	2.10	0.3	13	2.22	0.2	8	2.30	0.3	4	2.07	0.2	1
-5	2.32	0.2	2.08	0.2	10	2.11	0.1	9	2.25	0.2	3	2.08	0.2	0
-1	2.073	0.05	1.991	0.06	4	2.00	0.2	4	2.22	0.2	7	1.975	0.09	0.8
0	2.04	0.1	1.944	0.04	5	1.95	0.1	4	2.08	0.1	2	1.878	0.04	3
1	1.895	0.07	1.882	0.05	0.7	1.902	0.09	4	1.930	0.06	2	1.850	0.05	2
2	1.848	0.07	1.864	0.04	0.9	1.95	0.1	6	1.81	0.2	2	1.869	0.03	0.3
3	1.832	0.07	1.842	0.05	0.5	1.86	0.1	2	1.84	0.2	0.4	1.860	0.03	1
4	1.825	0.07	1.85	0.1	1	1.83	0.1	0.3	1.83	0.2	0.3	1.848	0.04	0.1
5	1.823	0.08	1.85	0.1	1	1.80	0.1	1	1.81	0.2	0.7	1.838	0.04	0.6
6	1.836	0.08	1.84	0.1	0.2	1.841	0.08	0.3	1.79	0.2	3	1.839	0.04	0.05
7	1.835	0.08	1.84	0.1	0.3	1.841	0.08	0.3	1.77	0.1	4	1.831	0.04	0.5
8	1.833	0.08	1.85	0.1	0.9	1.824	0.09	0.5	1.75	0.1	5	1.825	0.04	1
9	1.832	0.08	1.84	0.1	0.4	1.81	0.1	1	1.73	0.1	6	1.819	0.04	1
10	1.830	0.09	1.84	0.1	0.5	1.80	0.1	2	1.72	0.1	6	1.814	0.04	1
20	1.81	0.1	1.81	0.2	0	1.72	0.2	5	1.64	0.2	9	1.784	0.05	1
30	1.80	0.1	1.78	0.2	1	1.61	0.2	11	1.62	0.2	10	1.771	0.05	0.5
40	1.79	0.1	1.78	0.2	0.6	1.64	0.2	8	1.62	0.2	9	1.763	0.06	1

sensitive to reasonable choices of  $(l_{\min}, l_{\max})$ .

Examples are given for  $y_1$  in Figs. 13 ( $q = -25$ ), 14 ( $q = 2$ ), and 15 ( $q = 40$ ). For  $q = -25$ , the accuracy is very poor, as exhibited in the first line of Table I where  $\sigma_D/D_q$  are 17%, 19%, 8%, 17%, and 14% in columns 1, 2, 3, 4, and 5, respectively. Although we might claim that these results are too inaccurate to make sense, they are provided as a limit case for  $q$  small. This behavior is typical of a Grassberger-Procaccia algorithm. It is due to the fact that smaller  $q$ 's probe parts of the attractor where the measure is most rarefied, leading to poor statistics with fixed radii. However, evaluation of  $D_q$ 's ( $q < 1$ ) appears to be feasible although with poor accuracy. A

summary of  $D_q$ 's results is given in Fig. 16 and Table I. This table also provides  $\epsilon\%$ , the relative difference between  $D_q$ 's in  $\mathbb{R}^{25}$  and  $D_q$ 's in  $\mathbb{R}^3$ . Focusing on  $q > 1$  for which the algorithm is the most efficient, we conclude that the best reconstruction has been obtained with  $y_1$  (by examining both relative differences  $\epsilon\%$  and standard mean deviations  $\sigma_D$ ).

The Lyapunov spectrum of a 3D continuous dissipative chaotic system is of the kind  $(+, 0, -)$ .<sup>64</sup> Associating a partial dimension  $D_2^+ = 1$  with the positive Lyapunov exponent of the unstable direction,<sup>39</sup> another partial dimension  $D_2^0 = 1$  with the null Lyapunov exponent associated with the direction tangent to the flow,

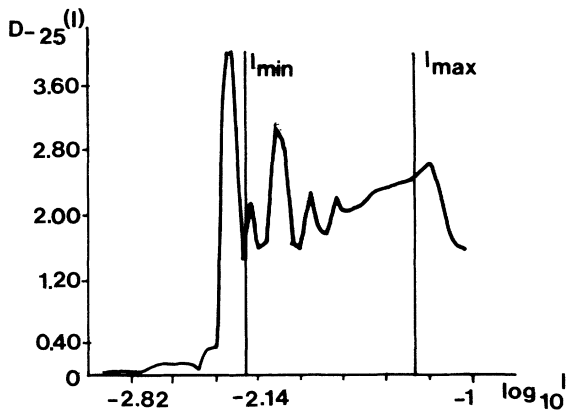


FIG. 13.  $D_{-25}(l)$  for reconstructed attractor in  $\mathbb{R}^{25}$  with variable  $y_1$ .

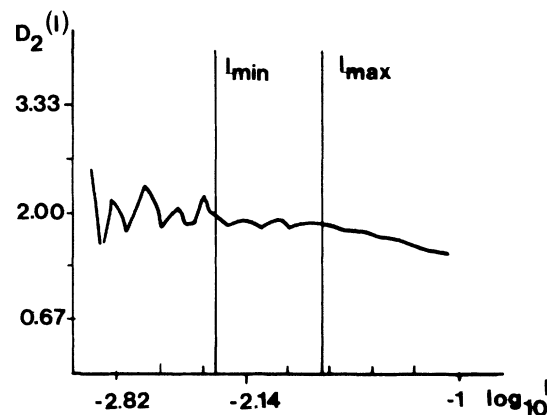


FIG. 14.  $D_2(l)$  for reconstructed attractor in  $\mathbb{R}^{25}$ . Variable  $y_1$ .

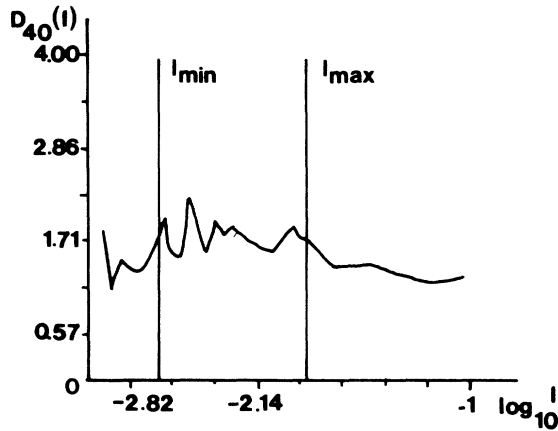


FIG. 15.  $D_{40}(l)$  for reconstructed attractor in  $\mathbb{R}^{25}$ . Variable  $y_1$ .

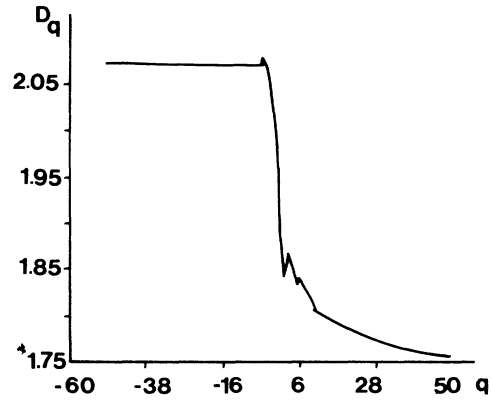


FIG. 17.  $D_q$  vs  $q$  in  $\mathbb{R}^{25}$  with  $y_1$ . High-resolution computation.

and another one  $D_2^- < 1$  with the negative Lyapunov exponent of the stable direction, we might expect  $D_2 = \sum_j D_2^j > 2$ .

On the other hand, most data in Table I lead to the conclusion that  $D_2 < 2$  both in  $\mathbb{R}^3$  and in  $\mathbb{R}^{25}$ , except for columns 3 (variable  $y_2$ ,  $1.85 < D_2 < 2.05$ ) and 4 (variable  $y_3$ ,  $1.61 < D_2 < 2.01$ ) but inaccuracies  $\sigma_D/D_q$  are very high for these columns. The fact that  $D_2 < 2$  also for computations in  $\mathbb{R}^3$  prevents us from invoking a poor determination of the optimal phase-space dimension  $n_0 = 25$ . We may, however, invoke an underestimate of the  $D_2$  value. A first reason may be difficulties inherent to the algorithm. Quantitatively, if we consider data in column 1, an underestimate by only about 5% would be enough to explain the discrepancy. But also, independently of algorithmic difficulties, we may invoke additional problems inherent to the structure of the attractor. Figure 9 shows that the attractor rests on two very flat

bands associated with the cutoff relation (50). Visually, these bands look like a Cantor structure contained in a plane, i.e., local (pointwise) dimensions could be expected to be smaller than 2 in these regions. This statement, however, relies on a visual feeling which is associated with large scales  $l$  chosen to plot the attractor. Due to the sharpness of the cutoff, we might also think that the attractor is there highly compressed in the direction perpendicular to the bands. It means that pointwise dimensions could be larger than 2 but that the attractor should be investigated at very small scales to resolve the fractal structure in the direction perpendicular to the bands. We remember that  $D_q$  computations ideally require us to take the limit  $l \rightarrow 0$  which is in practice forbidden. Therefore the existence of highly compressed bands would enhance the difficulties associated with this ideal requirement  $l \rightarrow 0$ . For this reason,  $D_q$  computations may have no meaning if we do not specify the scales used for the evaluation. We are able to determine  $D_q(l)$  but

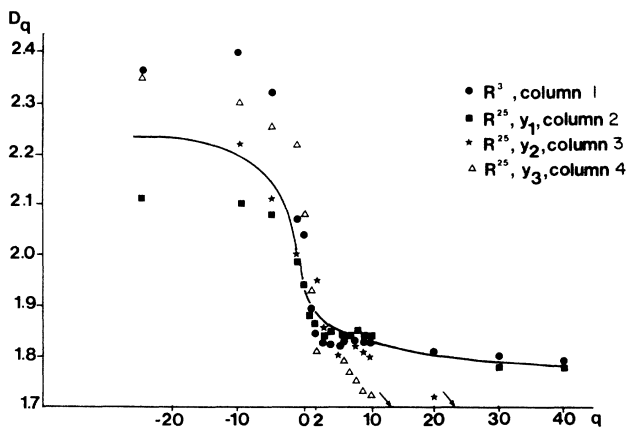


FIG. 16.  $D_q$  vs  $q$ , in  $\mathbb{R}^3$  and in  $\mathbb{R}^{25}$  (Table I, columns 1–4). Symbols are placed by starting for computations in  $\mathbb{R}^3$ , then for computations in  $\mathbb{R}^{25}$  with  $y_1, y_2, y_3$  successively. Symbols are omitted when they would overwrite previous ones. Note expanded vertical scales. Smoothing follows results in  $\mathbb{R}^3$  and in  $\mathbb{R}^{25}$  for  $y_1$ .

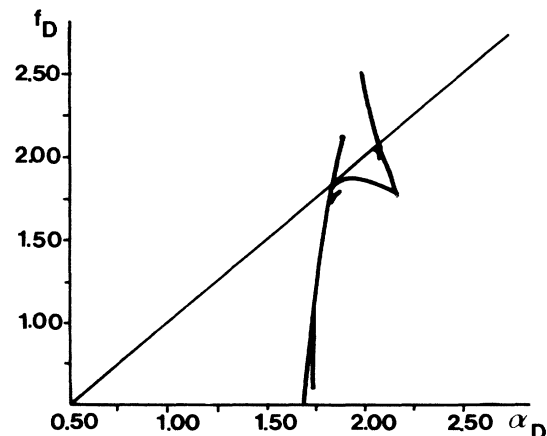


FIG. 18. An evaluation of singularity spectrum  $f_D(\alpha_D)$  with artifacts.

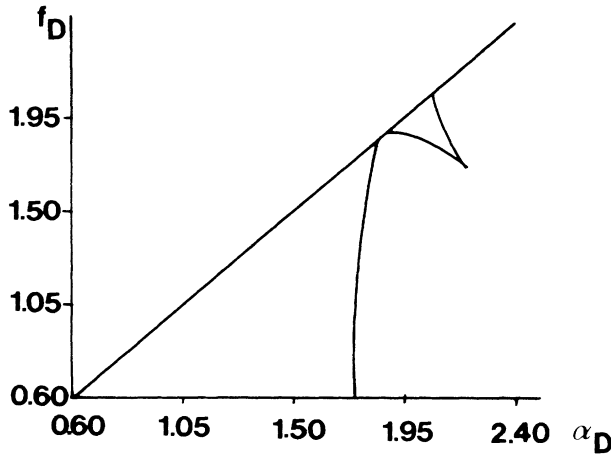


FIG. 19. An evaluation of singularity spectrum  $f_D(\alpha_D)$  after smoothing of the  $D_q$ 's. A last artifact branch still appears.

unable to determine  $D_q = \lim_{l \rightarrow 0} D_q(l)$ . For some attractors like the one in Fig. 9, this difficulty might be enhanced by a scale gap between large scales relevant in most parts of the object and much smaller scales relevant in squeezed parts like the aforementioned bands. This discussion can be given another basis by invoking the concept of effective dimension (Ref. 65, pp. 17 and 18), i.e., a dimension which is not determined for  $l \rightarrow 0$  but for a scale relevant to the location of the observer with respect to the object or equivalently for a scale relevant to the visual feeling of the object. The situation might be similar in the case of the Rössler attractor<sup>2</sup> containing a spiraling band which appears to remain in a plane near to and parallel to the  $(x, y)$  plane. For this case, Landa and Rozenblyum<sup>66</sup> claims  $D_2 = 1.88 \pm 0.03$  for an evaluation carried out on the original attractor in  $\mathbb{R}^3$ . We now remember that increasing  $q$  is equivalent to probe parts of the attractor where the measure is more concentrated. If the measure is more concentrated in the cutoff bands, then  $D_q$  ( $q > 2$ ) progressively give us a better estimate of effective pointwise dimensions in these bands (see Table I). Conversely, for  $D_q$  ( $q < 2$ ), we progressively probe parts of the attractor outside of these bands and find that  $D_q$  becomes larger than 2. We must finally also mention

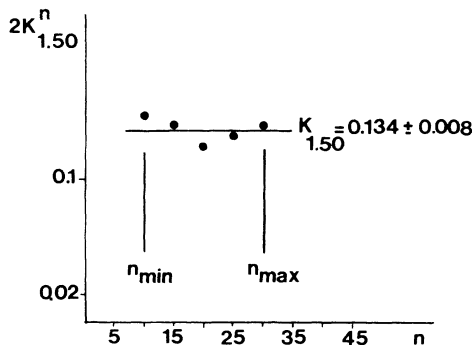


FIG. 20.  $K_q^n/Q$ ,  $q=1.50$ , vs  $n$ ,  $l=0.0019$ .

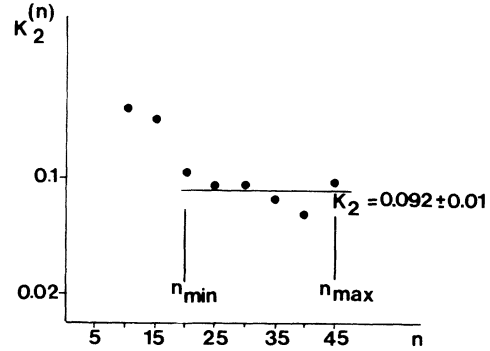


FIG. 21.  $K_q^n/Q$ ,  $q=2$ , vs  $n$ ,  $l=0.0019$ .

the possibility of a lack of hyperbolicity of the attractor leading to phase-transition-like phenomena. Such a lack of hyperbolicity leads to the creation of heavy boxes with small dimensions. For instance, the smallest singularity index in the Hénon 2D map is  $\alpha_{\min} \approx 0.85 < 1$ . If this map were lifted to a 3D flow, we would obtain pointwise dimensions  $1.85 < 2$  for the heaviest boxes. This discussion shows that, due to the existence of sharp cutoff bands, the attractor in Fig. 9 is an interesting object which should be more extensively studied in its own right. Such a study is, however, outside of the scope of this paper.

Finally, to determine the singularity spectrum  $f_D(\alpha_D)$ , we compute again  $D_q$ 's with, however, a small step  $\Delta q = 0.25$  and very high resolution  $(N, m) = (2 \times 10^6, 2000)$  for the sake of accuracy. To save storage, computations are carried out in  $\mathbb{R}^{25}$ . We used the best variable  $y_1$  as discussed from Table I. The increase of accuracy with respect to the previous run at small resolution is very apparent for  $q > 1$ , up to a decrease of  $\sigma_D$  by a factor 4 (see last column in Table I). The resulting  $D_q$ 's are shown in Fig. 17. We observe some accidents in which, for instance, relation (61) is not satisfied. They are associated with modification of the scaling domains  $(l_{\min}, l_{\max})$  which depend on  $q$ . Legendre transforming these data [(relation (62))], we obtain the spectrum of Fig. 18 which, however, contains artifacts produced by accidents in Fig. 17. The overall theoretical shape of a  $f_D(\alpha_D)$  spectrum is, however, well recog-

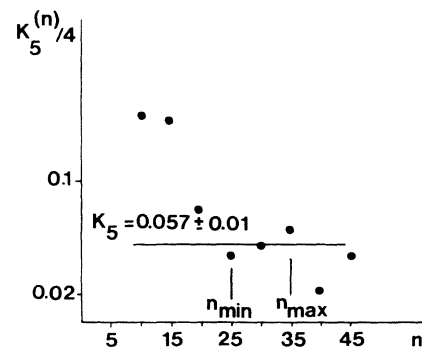
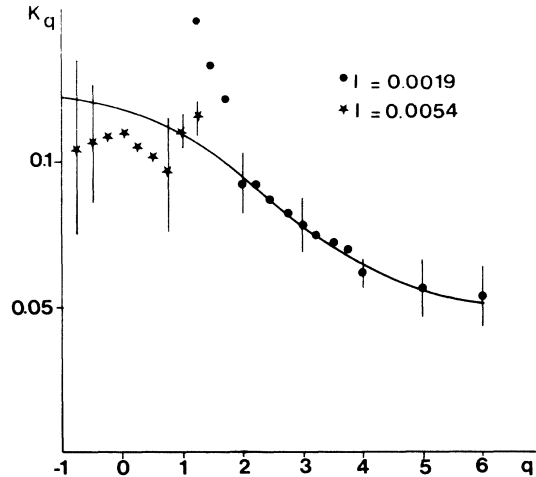


FIG. 22.  $K_q^n/Q$ ,  $q=5$ , vs  $n$ ,  $l=0.0019$ .

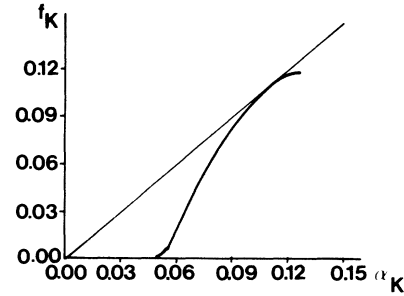
FIG. 23.  $K_q$  vs  $q$ .

nized.<sup>54,55</sup> After smoothing data from Fig. 17, we obtain the spectrum displayed in Fig. 19. There remains an artifact branch for large  $\alpha$ 's associated with an excess of flatness at small  $q$ 's in Fig. 17. We note that, in both Figs. 18 and 19, the bisector line is tangent to the spectrum as it should be. This occurs for  $q=1$  with  $\alpha_D(1)=f_D[\alpha_D(1)]=D_1$  [relation (62)]. The maximum  $f_D(\alpha_D)$  of the nonartifact convex part of the profile indicates  $f_D=D_0$ , the Hausdorff dimension of the set.

#### D. Dynamical properties of a HBE attractor

$K_q$ 's are computed in  $\mathbb{R}^{25}$  for the best variable  $y_1$ . Distance  $l$  in (67) is taken equal to 0.0054 and 0.0019 for  $q \leq 1.25$  and  $q \geq 1.25$ , respectively, corresponding to the arithmetic average of logarithms of the scaling domain frontiers  $l_{\min}$  and  $l_{\max}$  in  $D_q$  computations at very high resolution. Increment  $s$  is 3. After preliminary runs, a final run is carried out with  $\Delta q=0.25$ , a high resolution  $(N, m)=(2 \times 10^6, 2000)$ ,  $p=24$ ,  $\Delta t=0.05$  and  $n$  increased from 10 to 45. The window length  $(n-1)p\Delta t$  then ranges from about  $4T_0$  to  $20T_0$ , in which  $T_0$  is again a typical pseudoperiod.

Figures 20–22 show examples of  $K_q^n/Q$  [relation (68)] for  $q=1.50$ , 2, and 5 with  $l=0.0019$ . Accounting for the fact that  $K_q$  computations are notoriously more difficult than for  $D_q$ 's, the quality of the plateau is not very bad for  $q=2$  leading to  $K_q=0.092$  with  $\sigma_K=0.01$ . For  $q=1.50$ , an evaluation of  $K_q$  is also possible but becomes very insecure for smaller  $q$ 's. For  $q > 2$ , deterioration of the plateau is very fast as exemplified in Fig. 22 for  $q=5$ . Values of  $[n_{\min}, n_{\max}]$  used for averaging  $K_q^n/Q$  are also indicated in figures. Similarly, a few  $K_q$ 's ( $q \leq 1.25$ ) can be evaluated with  $l=0.0054$  but only on a very limited range of  $q$ 's. Limiting our results to the cases when  $\sigma_K/K_q$  is smaller than about 25%, we obtain data given in Fig. 23. Legendre transforming, we obtain

FIG. 24. Singularity spectrum  $f_K(\alpha_K)$ .

a singularity spectrum  $f_K(\alpha_K)$  shown in Fig. 24. We omitted an artifact of negative  $f_K$ 's at small  $\alpha_K$ 's associated with inaccuracies in  $K_q$ 's at large  $q$ 's in Fig. 23. Again, the bisector line is tangent to  $f_K(\alpha_K)$  as it should be, but the right downward branch of the profile is nearly fully missed.

## VI. CONCLUSION

This paper has been devoted to the understanding of a new dissipative nonlinear thermodynamical system in which heating a liquid below a free surface by using a laser (HBE's) or a hot wire (HWE's) produces a rich set of bifurcations up to chaos. Although too complex to handle correctly the PDE's defining it, the true system can be reduced to a model dynamical system with two controls evolving in a 3D phase space. The agreement between the true system and the model is very good for the first bifurcation of the system (a Hopf bifurcation). For secondary instabilities, the true system and model show a fair resemblance, leading us to the conclusion that we have reached a good understanding of thermal lens oscillations and associated hot-wire experiments, at least much better than hitherto possible, with a remarkable economy of mathematical tools. The lack of quasiperiodicity and associated hysteresis in the model, however, indicates that some physical ingredients remain to be identified. Also, metric and dynamical properties (generalized dimensions and entropies, and associated singularity spectra) of a strange chaotic attractor generated by the model have been investigated. Due to the existence of sharp cutoff bands, this attractor appears to be an interesting object for which the interest of an extensive study in its own right is warranted.

## ACKNOWLEDGMENTS

The Laboratoire d'Energétique des Systèmes et Procédés is a part of the "Unité no. 230" associated with the Centre National de la Recherche Scientifique, France (National Center for Scientific Research). The aid of C. Rozé for checking some computations in this work is also acknowledged.

- <sup>1</sup>J. Guckenheimer and P. Holmes, *Nonlinear Oscillations, Dynamical Systems, and Bifurcations of Vector Fields*, Vol. 42 of *Applied Mathematical Sciences*, edited by F. John, J. E. Marsden, and L. Sirovich (Springer-Verlag, New York, 1983).
- <sup>2</sup>J. M. T. Thompson and H. B. Stewart, *Nonlinear Dynamics and Chaos* (Wiley, New York, 1987).
- <sup>3</sup>R. L. Devaney, *An Introduction to Chaotic Dynamical Systems* (Addison-Wesley, Reading, MA, 1987).
- <sup>4</sup>P. Bergé, Y. Pomeau, and C. Vidal, *L'ordre dans le chaos* (Hermann, Paris, 1984).
- <sup>5</sup>*Convective Transport and Instability Phenomena*, edited by J. Zierep and H. Oertel (Braun, Karlsruhe, 1982).
- <sup>6</sup>E. Jakeman, E. R. Pike, and J. M. Vaughan, R. R. E. Newsletter and Research Review No. 12, 1973 (unpublished).
- <sup>7</sup>R. Anthore, P. Flament, G. Gouesbet, M. Rhazi, and M. E. Weill, *Appl. Opt.* **21**, 2 (1982).
- <sup>8</sup>G. Gouesbet, M. Rhazi, and M. E. Weill, *Appl. Opt.* **22**, 304 (1983).
- <sup>9</sup>G. Gouesbet and E. Lefort, *Phys. Rev. A* **37**, 4903 (1988).
- <sup>10</sup>M. E. Weill, M. Rhazi, and G. Gouesbet, *J. Phys. (Paris)* **46**, 1501 (1985).
- <sup>11</sup>G. Gouesbet, M. E. Weill, and E. Lefort, *AIAA J.* **24**, 1324 (1986).
- <sup>12</sup>J. Horák, *Fortschr. Phys.* **37**, 1 (1989).
- <sup>13</sup>A. Arneodo and O. Thual, *Le Chaos* (Eyrolles, Paris, 1988).
- <sup>14</sup>G. Gouesbet, *JSME Int. J. Ser. II*, **32**, 301 (1989).
- <sup>15</sup>G. Gouesbet and E. Lefort, *Dynamical States in Thermal Lensing* (American Institute of Aeronautics and Astronautics, Washington, D. C., 1988).
- <sup>16</sup>G. Gouesbet and E. Lefort, *Appl. Opt.* **26**, 2940 (1987).
- <sup>17</sup>M. E. Weill, M. Rhazi, and G. Gouesbet, *C. R. Acad. Sci. Paris Sér. II* **294**, 567 (1982).
- <sup>18</sup>G. Gouesbet, *Physico Chem. Hydrodyn.* **8**, 349 (1987).
- <sup>19</sup>W. V. Kayser and J. C. Berg, *J. Fluid Mech.* **57**, 739 (1973).
- <sup>20</sup>J. Maquet, G. Gouesbet, and A. Berlemont, in *Proceedings of the 5th International Conference on Numerical Methods for Thermal Problems, Montréal, Canada, 1987*, edited by R. W. Lewis, K. Morgan, and W. G. Habashi (Pineridge, Swansea, UK, 1987), Vol. 5, Pt. 1, pp. 472–483.
- <sup>21</sup>G. Gouesbet and J. Maquet, *Overstability for Surface Tension and Coupled Buoyancy-Driven Instability in a Horizontal Liquid Layer. Toward the Understanding of Thermal Lens Oscillations* (American Institute of Aeronautics and Astronautics, New York, 1987).
- <sup>22</sup>G. Gouesbet and J. Maquet, *AIAA J. Thermophys. Heat Transfer* **3**, 27 (1989).
- <sup>23</sup>G. Gouesbet, J. Maquet, C. Rozé, and R. Darrigo, *Phys. Fluids* (to be published).
- <sup>24</sup>C. Rozé, G. Gouesbet, and J. Maquet, *Overstability Under Simultaneous Surface Tension, Buoyancy and Shear Effects in a Horizontal Liquid Layer* (American Institute of Aeronautics and Astronautics, Washington, D. C., 1990).
- <sup>25</sup>G. Gouesbet and J. Maquet, *Commun. Int. J. Heat and Mass Transfer* **16**, 133 (1989).
- <sup>26</sup>G. Gouesbet, *Dynamical States and Bifurcations in a New Thermo-dynamical Nonlinear System: Optical Heartbeats and Associated Phenomena* [*Entropie* **153/154**, 47 (1990)].
- <sup>27</sup>H. B. Stewart (unpublished).
- <sup>28</sup>V. Yu. Bazhenov, M. V. Vasnetsov, M. S. Soskin, and V. B. Taremenko, *Pis'ma Zh. Eksp. Teor. Fiz.* **49**, 330 (1989) [*JETP Lett.* **49**, 376 (1989)].
- <sup>29</sup>P. Grassberger, *Phys. Lett.* **97A**, 227 (1983).
- <sup>30</sup>H. G. E. Hentschel and I. Procaccia, *Physica D* **8**, 435 (1983).
- <sup>31</sup>P. Grassberger and I. Procaccia, *Physica D* **13**, 34 (1984).
- <sup>32</sup>R. Badii and A. Politi, *J. Stat. Phys.* **40**, 725 (1985).
- <sup>33</sup>A. Cohen, I. Procaccia, *Physical Review A* **31**, 3, 1872 (1985).
- <sup>34</sup>J. D. Farmer, E. Ott, J. A. Yorke, *Physica* **7D**, 153 (1983).
- <sup>35</sup>H. S. Greenside, A. Wolf, J. Swift, T. Pignataro, *Physical Review A* **25**, 6, 3453 (1982).
- <sup>36</sup>R. Mané, in *Dynamical Systems and Turbulence*, Vol. 898 of *Lecture Notes in Mathematics*, edited by D. A. Rand and L. S. Young (Springer-Verlag, New York, 1981), pp. 230–242.
- <sup>37</sup>F. Takens, in Ref. 36, pp. 366–381.
- <sup>38</sup>F. Takens, in *Nonlinear Dynamics and Turbulence*, edited by G. I. Barenblatt, G. Iooss, and D. D. Joseph (Pitman, New York, 1983), pp. 314–332.
- <sup>39</sup>P. Grassberger, R. Badii, and A. Politi, *J. Stat. Phys.* **51**, 135 (1988).
- <sup>40</sup>P. Cvitanovic, *Phys. Rev. Lett.* **61**, 2729 (1988).
- <sup>41</sup>T. Morita, H. Hata, H. Mori, T. Horita, and K. Tomita, *Prog. Theor. Phys.* **79**, 296 (1988).
- <sup>42</sup>C. Grebogi, E. Ott, and J. A. Yorke, *Phys. Rev. A* **37**, 1711 (1988).
- <sup>43</sup>D. Auerbach, Ben O'Shaughnessy, and I. Procaccia, *Phys. Rev. A* **37**, 2234 (1988).
- <sup>44</sup>W. Van de Water and P. Schram, *Phys. Rev. A* **37**, 3118 (1988).
- <sup>45</sup>G. Broggi, *J. Opt. Soc. Am. B* **5**, 1020 (1988).
- <sup>46</sup>R. Badii and G. Broggi, *Phys. Lett. A* **131**, 339 (1988).
- <sup>47</sup>M. Ravani, B. Derighetti, G. Broggi, and E. Brun, *J. Opt. Soc. Am. B* **5**, 1029 (1988).
- <sup>48</sup>P. Grassberger and I. Procaccia, *Phys. Rev. Lett.* **50**, 346 (1983).
- <sup>49</sup>P. Grassberger and I. Procaccia, *Phys. Rev. A* **28**, 2591 (1983).
- <sup>50</sup>B. Malraison, P. Atten, P. Bergé, M. Dubois, *C. R. Acad. Sci. Paris, Ser. II*, **297**, 209 (1983).
- <sup>51</sup>B. Malraison, P. Atten, P. Bergé, and M. Dubois, *J. Phys. (Paris) Lett.* **44**, L897 (1983).
- <sup>52</sup>P. Atten, J. G. Caputo, B. Malraison, and Y. Gagne, *J. Mec. Theor. Appl.* **133**, special issue (1984).
- <sup>53</sup>J. G. Caputo and P. Atten, *Phys. Rev. A* **35**, 1311 (1987).
- <sup>54</sup>T. C. Halsey, M. H. Jensen, L. P. Kadanoff, I. Procaccia, and B. I. Shraiman, *Phys. Rev. A* **33**, 1141 (1986).
- <sup>55</sup>J. P. Eckmann and I. Procaccia, *Phys. Rev. A* **34**, 659 (1986).
- <sup>56</sup>A. Politi, R. Badii, and P. Grassberger, *J. Phys. A: Math. Gen.* **21**, L763 (1988).
- <sup>57</sup>E. Ott, C. Grebogi, and J. A. Yorke, *Phys. Lett. A* **135**, 343 (1989).
- <sup>58</sup>C. Grebogi, E. Ott, S. Pelikan, and J. A. Yorke, *Physica D* **13**, 261 (1984).
- <sup>59</sup>Y. Termonia, *Phys. Rev. A* **28**, 2591 (1983).
- <sup>60</sup>Y. Termonia, *Phys. Rev. A* **29**, 1612 (1984).
- <sup>61</sup>A. Arneodo, G. Grasseau, and E. J. Kostelich, *Phys. Lett. A* **124**, 426 (1987).
- <sup>62</sup>A. M. Albano, J. Muench, and C. Schwartz, *Phys. Rev. A* **38**, 3017 (1988).
- <sup>63</sup>A. M. Fraser, *Physica D* **34**, 391 (1989).
- <sup>64</sup>A. Wolf, J. B. Swift, H. L. Swinney, and J. A. Vastano, *Physica D* **16**, 285 (1985).
- <sup>65</sup>B. B. Mandelbrot, *The Fractal Geometry of Nature* (Freeman, New York, 1983).
- <sup>66</sup>P. S. Landa and M. G. Rozenblyum, *Zh. Tekh. Fiz.* **59**, 13 (1989) [*Sov. Phys.—Tech. Phys.* **34**, 1989].